EUROPEAN ORGANIZATION FOR NUCLEAR RESEARCH

CERN/EP 87-31
17 February 1987

The European Hybrid Spectrometer

LEBC – EHS Collaboration

Aachen[1], Berlin[2], Bombay[3], Brussel[4], CERN[5], College de France[6], Duke[7], Genova[8], Tokyo[9], Liverpool[10], Madrid[11], Mons[12], Oxford[13], Padova[14], Paris[15], Rome[16], Rutherford[17], Rutgers[18], Serpukov[19], Stockholm[20], Strasbourg[21], Trieste[20], Vienna[23]

M.Aguilar – Benitez[11] , W.W.M.Allison[13] , A.deAngelis[14] , M.Atkinsson[18] , J.L.Bailly[12] , W.Bartl[23] , M.Begalli[1] ,
A.Bettini[14] , R.Bizzarri[16] , C.Brooks[13] , R.Brun[5] , V.Canale[16] , E.diCapua[16] , C.Caso[8] , E.Castelli[22] , P.Checcia[14] ,
N.Colino[11] , S.J.Colwill[13] , R.Contri[8] , D.Crennell[18] , C.Defoix[6] , F.Diez – Hedo[11] , J.Dolbeau[6] , J.Duboc[15] ,
J.Dumarchez[15] , I.Duran[11] , B.Epp[23] , M.Eriksson[20] , S.Falciano[16] , C.Fernandez[5] , C.Fisher[18] , Y.V.Fisjak[19] ,
F.Fontanelli[8] , U.Gasparini[14] , U.Gensch[2] , S.Gentile[16] , D.B.Gibaut[13] , L.Haupt[20] , S.Hellman[20] , J.J.Hernandez[5] ,
Ph.Herquet[12] , A.Herve[5] , S.O.Holmgren[20] , J.Hrubec[23] , P.Hughes[18] , D.Huss[21] , M.Iori[16] , Y.M.Ivanyushenkov[19] ,
E.Jegham[21] , K.E.Johansson[20] , M.I.Josa[11] , J.Kesteman[12] , A.G.Kholodenko[19] , E.P.Kistenev[19] , D.Knauss[2] ,
P.Ladron de Guevara[11] , H.Leutz[5] , M.MacDermott[18] , M.Mazzucato[14] , A.Michalon[21] , M.E.Michalon – Mentzer[21] ,
N.G.Minaev[19] , T.Moa[20] , R.Monge[8] , L.Montanet[5] , T.Naumann[2] , G.Neuhofer[23] , S.Nilsson[20] , H.Nowak[2] , G.Otter[1] ,
R.Ouared[15] , J.Panella[13] , M.Pernicka[23] , O.Pingot[12] , G.Piredda[16] , B.F.Polyakov[19] , A.Poppleton[5] , P.Poropat[22] ,
B.Powell[5] , S.Reucroft[5] , H.Rohringer[23] , A.Roth[1] , J.Salicio[11] , J.Schmidmeyer[23] , R.Schulte[1] , B.Sellden[20] ,
M.Sessa[22] , P.D.Shields[13] , S.Squarcia[8] , E.A.Starchenko[19] , W.Strusczinski[1] , M.C.Touboul[15] , U.Trevisan[8] ,
C.Troncon[22] , L.Ventura[14] , P.Vilain[4] , E.V.Vlasov[19] , C.Voltolini[21] , B.Vonck[4] , P.R.S.Wright[5] and G.Zumerle[14]

Submitted to Nuclear Instruments and Methods in Physics Research

LHT/lht

1 III.Physikalisches Inst. der Technischen Hochschule, D – 5100 Aachen, Federal Republic of Germany

2 Tata Institute of Fundamental Research, Bombay 400 005, India

3 Institut fur Hochenergiephysik der AdW der DDR, Berlin – Zeuthen, GDR

4 Vrije Univ. Brussel (VUB), B – 1050 Brussel, Belgium

5 CERN, European Organisation for Nuclear Research, CH – 1211 Geneva 23, Switzerland

6 Lab. de Physique Corpusculaire, College de France, F – 75231 Paris Cedex 05, France

7 Physics Department, Duke University, Durham, North Carolina 27706, USA

8 Dipartimento di Fisica, Universita di Genova, Italy

9 Tokyo University of Agriculture and Technology, High Energy Group, Koganei, Tokyo and Tokyo Metropolitan University, Tokyo 158, Japan

10 Oliver Lodge Lab., University of Liverpool, GB – Liverpool L69, 3RH, England

11 Grupo de Altas Energias, Junta de Energia Nuclear, E – Madrid 3, Spain

12 Physique des Particules Elementaires, Universite de l'Etat a Mons, B – 7000 Mons, Belgique

13 Nuclear Physics Laboratory, University of Oxford, GB – Oxford OX1 3RH, England

14 Dipartimento di Fisica, Universita di Padova, I – 35131 Padova, Italy

15 Lab. de Physique Nucleaire et des Hautes Energies, Univ. Pierre et Marie Curie, F – 75231 Paris Cedex 05, France

16 Dipartimento di Fisica, Universita di Roma, 'La Sapienza', I – 00185 Roma, Italy

17 Rutgers University, Department of Physics, New Brunswick, NJ – 08903, USA

18 Rutherford and Appleton Laboratory, Chilton, GB – Didcot, OX11 0QX, England

19 Institut for High Energy Physics, Serpukov, 142284 Protvino, USSR

20 Institute of Physics, University of Stockholm, S – 113 46 Stockholm, Sweden

21 Division des Hautes Energies CRN Strasbourg and Louis Pasteur, BP 20 CR, F – 67037 Strasbourg Cedex, France

22 Istituto di Fisica, Universita di Trieste, I – 34100 Trieste, Italy

23 Institut fur Hochenergiephysik der Oesterreichischen Akademie der Wissenschaften, A – 1050 Wien, Austria.

Abstract

The final version of the European Hybrid Spectrometer (EHS) is described. EHS was used in the NA27 Experiment to study charm particles produced in 360 GeV/c π^-p and 400 GeV/c pp interactions. A rapid cycling, high resolution bubble chamber (LEBC) produced bubbles of 17 μm diameter which were measured with a precision of 2.5 μm. Shortlived charm particles are observed with an efficiency up to 90% ($D^{\pm}$). The spectrometer accepts 70 % of all particles produced, including approximately 100% of those in the forward hemisphere and the momenta of charged particles are measured to better than 1% over the whole momentum range. The charged particle identification detectors give information on 84% of the spectrometer tracks, half of which obtain unique identification. Two lead glass detectors measure the energy of electromagnetic showers such that the π^0 mass distribution has a FWHM of 20 MeV/c^2. Hadronic showers are measured with two iron/scintillator calorimeters. The mass resolutions are 3.0, 0.9 and 11 MeV/c^2 for K^0, Λ^0 and $D^0 \rightarrow$ charged particles respectively. The D^0 mass is measured to be 1865.1 $\pm$ 1.8 $\pm$ 0.8 MeV/c^2.

1 Introduction

On 28 May 1984, the Lexan Bubble Chamber (LEBC) was stopped after having taken more than two million pictures of proton−proton interactions for the NA27 Experiment in the North Area of the CERN 450 GeV/c Super Proton Synchrotron (SPS). The experiment was carried out by the LEBC−EHS Collaboration in order to measure the lifetime of the D, D_s and Λ_c particles and to study their hadronic production properties.

NA27 is one of the most complex bubble chamber experiments ever made and the last one in a series of experiments using the European Hybrid Spectrometer (EHS) to analyse the secondary particles produced in high energy hadron collisions.

EHS was proposed to the SPSC in 1974 [1]. The aim was to provide the physics community with a general facility for the study of strong interactions in the energy range accessible with the accelerator under construction. Different targets and vertex detectors were to be coupled with a downstream spectrometer with large geometrical acceptance, good momentum resolution and charged and neutral particle identification in a wide momentum range. In particular, strange particle production was to be studied in detail at a beam momentum of 200 GeV/c, using the Rapid Cycling Bubble Chamber (RCBC) with about 1 m fiducial length as vertex detector.

However, during the construction of EHS, new theoretical and experimental results on charm particle production and decay properties appeared, and motivated in 1979 a proposal to study these particles in detail, using the available parts of EHS together with a high resolution hydrogen bubble chamber [2]. That version of the apparatus, used in the experiment called NA16, is described in detail in ref. [3].

Charm particles produced in hadron collisions at SPS energies have production cross sections of the order of 10 μb, and the final states of charm events contain on the average more than 12 charged particles. Lifetimes for the charm particles of the order of a few times 10^{-13} s give an average decay length in the laboratory of $\approx$ 3 mm, and a transverse decay distance from the beam direction of $<$ 1 mm. The impact parameter at the primary vertex of tracks from charm decays has an average of 50 μm.

Guided by these facts, an improved bubble chamber and spectrometer were exposed in 1982 to a 360 GeV/c π^- beam for the NA27 Experiment, giving a sensitivity of 15.8 events/μb [4]. The same collaboration collected in two 400 GeV/c proton exposures a total of 2.3 million pictures and obtained a sensitivity of 38.5 events/μb with a further developed spectrometer. This final version of the apparatus is described here.

Other experiments having used the whole or parts of EHS with RCBC as vertex detector are :

- NA22, which study hadronic interactions with $\pi^+/K^+/p$ beams at 250 GeV/c [5], and
- NA23, which study diffractive dissociation, especially into strange particles [6] .

The paper is organised as follows. In sect. 2, the experimental arrangement is presented. Sect. 3 describes the procedures used in track and event reconstruction, and sect. 4 deals with the particle identification. In sect. 5 we give examples of how the detectors have been used to reconstruct charm particles, and sect. 6 contains some concluding remarks.

In the whole report, emphasis is given to new or modified items, and those already described in refs [2] or [4] are only summarized.

2 Experimental arrangement

2.1 General layout

The apparatus used in NA27 is shown in fig. 1, where the following groups of detectors are distinguished :

- the upstream lever arm for beam definition,
- the high resolution liquid hydrogen bubble chamber (LEBC) serving both as target and vertex detector,
- the zeroth lever arm with small high precision wire and drift chambers for triggering and track reconstruction,
- the first lever arm of detectors and a superconducting magnet (LA1),
- the second lever arm and a conventional C−magnet (LA2).

The first and the second lever arms contain drift chambers for measurement of particle trajectories, charged particle identification detectors and calorimeters for measurement of electromagnetic and hadronic showers.

Technical information for all detectors is given in tables 1 – 5. The coordinate system used to describe the detectors in EHS has the X – direction along the beam, Y vertically upwards and Z horizontally in a right – handed system with the origin in the centre of the bubble chamber. In the following, transverse dimensions are given as width × height (Z × Y).

2.2 Beam and upstream lever arm

EHS is situated in the H2 beam line, described in detail in ref. [7]. The beam consists of 400 GeV/c secondary protons with momentum bite $dp/p < 0.3\%$ and with an estimated contamination from other particles < 1%.

The flux from the target is set with collimators to give about 10^5 particles in the 2.8 s spill every 14 s. Two systems are used to limit the number of tracks in the bubble chamber and space charge effects in the drift chambers. A rotating collimator, synchronized with the expansion cycle of the bubble chamber, reduces the number of particles to about 7000 per spill. A fast kicker magnet system [8] removes primary particles just before the sensitive period of the bubble chamber cycle and when an interaction has been recorded, leaving about 1500 particles per spill during the sensitive time of the bubble chamber.

A quadrupole magnet 40 m upstream of LEBC gives the beam a horizontal focus of about 2 mm width and a vertical size and divergence of 4 cm and 0.1 mrad respectively at LEBC. In the last part of the NA27 proton run, another quadrupole 20 m upstream of LEBC focused the beam to within 1 mm to better match the depth of field of the bubble chamber optics.

The incident beam particles are measured by two Multi Wire Proportional Chambers (MWPC) and two Silicon Strip Detectors (SSD). The identical MWPC U1 and U3 have five wire planes each, giving a spatial precision of ≈ 250 μm . These chambers are further described in ref. [3].

The silicon detectors SSD0 and SSD1 both have 100 vertical strips with 100 μm pitch and a length of 3 cm. The strips are manufactured by p – type implantation on a 300 μm thick base of

n−type silicon. Working conditions for these chambers are summarized in table 6, and a detailed description of the design and operation is found in ref. [9].

The transverse coordinates of beam tracks in the bubble chamber are determined by the wire chambers to within 250 μm and the Z−coordinate by the silicon detectors to within 40 μm . The direction of beam tracks is measured to 0.02 mrad .

2.3 The Bubble chamber LEBC

LEBC is a rapid cycling liquid hydrogen bubble chamber, designed to detect particles with short lifetimes. It is basically of the same design as the chamber used in the π^- exposure, which was developed from the successful version used in NA16 [10]. A bubble diameter of less than 20 μm is desirable for high detection efficiency of charm particles, and with 30 Hz cycling rate, a good sensitivity would be obtained.

The photographed chamber volume, recorded on 50 mm film after a demagnification of 1:0.89, is 12 cm along the beam, ≈2.5 cm deep along the optical axis and 5 cm high. To obtain a high enough bubble density, the chamber is operated close to the foam limit, and constructed as a clean chamber without any seals or other parts which may cause parasitic boiling. The chamber operating conditions are listed in table 7.

The chamber body (fig. 2a) is built entirely from Lexan, which is transparent to visible light and sufficiently strong also at cryogenic temperatures. To allow for the highest possible optical resolution, LEBC is equipped with two optical windows for straight through illumination. The circular expansion membrane is located at the bottom of the chamber body and activated by a vertical hydraulic piston outside the chamber. This system controls both the static pressure of the hydrogen and the expansion cycle. The chamber is installed in a steel vacuum tank and supplied with liquid hydrogen from dewars. Heat radiation from the surroundings through the optical windows is minimized with goldplated windows. Fig. 2b shows the chamber mounted in its support.

The chamber is illuminated by a laser via two light guides, and the light is directed into the objective of the corresponding camera. Light which has been diffracted in the gas bubbles interferes with

the incident light to produce unexposed spots in the film. This diffractive bright field photography is superior to classical refractive photography in that the scattered light intensity is much higher, which results in a better contrast. Compared to holography it has the advantage of a simpler scanning procedure, a very important issue when three million pictures have to be analysed. Fig. 3 shows a bubble chamber picture of an event with two decaying neutral charm particles.

2.4 The zeroth lever arm

The reconstruction of space tracks from the bubble chamber track images relies on the hits in detectors close to LEBC, the zeroth lever arm, shown in fig. 4.

The two single plane wire chambers W0 and W1 are used both for track reconstruction and in the trigger. The working conditions are summarized in table 8, and details of the design and operation are found in ref. [9].

Two small drift chambers MDC1 and MDC2 are placed immediately downstream of the wire chambers W0 and W1 respectively. Fig. 5 shows a photograph of W0 and MDC1 mounted on the common support.

MDC1 has nine parallel drift cells, each with ten vertical sense wires spaced at 5 mm in the XY plane. The maximal drift length is 8 mm, giving a sensitive area of 14.4× 16.0 cm^2. The 10 μm diameter sense wires are stretched to 1 N in special guides to a positional accuracy of 15 μm.

The chamber is operated with a gas mixture of 75% propane and 25% ethylene at a relative pressure of 3.0 bar and with a high voltage of 9.8 kV. Particles enter and leave the chamber through two circular 250 μm thick mylar windows. The two−track resolution is $\approx$ 1 mm with a drift speed of 5 cm/μs. The electronics accept a varying number of hits on the wires, decreasing from six hits at the centre to one on the outer wires. Results obtained for a similar detector [11], indicate a resolution of 35 μm per space point.

MDC2 has a sensitive area of 30.4x30 cm^2 but is otherwise very similar to MDC1. It has 19 driftcells with 20 μm sense wires and carbon coated aluminised mylar foils for the cathode planes. It is run at 2 bar relative pressure and high voltage 9.0 kV.

The proportional inclined chamber (PIC12) is installed in the centre of the magnet M1. Two single plane modules are mounted with the wireplanes at 35° with respect to the vertical. For horizontal tracks, typically five independent drift time measurements give a spatial accuracy in the bending plane of ≈ 100 μm and a rough measurement of the inclination. The two track resolution is ≈ 500 μm, and for three or more tracks the resolution is of the order of the wire spacing, 2 mm. Further details are found in refs [3,12].

The new detector PIC34 is introduced just upstream of PIC12. It has the same construction as PIC12, except that the two sense wire planes are contained in one gas volume and have half the number of wires (320 wires in each plane).

2.5 The Spectrometer

Particle momenta are measured in two lever arms, each containing a magnet and three drift chambers giving space points with high precision along the trajectory of the particle. Slow particles, which are strongly deflected by the magnet M1, usually obtain their momentum measurement from the hits in the MWPC W2 and PIC close to the magnet. Particles with low and medium momenta ($\approx 2-30$ GeV/c), traverse the whole or part of lever arm one, and the trajectories are measured by the drift chambers D1 − D3. Medium and high momentum particles get additional momentum measurement from the magnet M2 and the three drift chambers D4 − D6 in lever arm two.

The large wire chamber W2 has been equipped with an additional seventh wire plane with vertical wires in order to improve the track reconstruction, and previously used wire cathode planes have been replaced by carbon coated mylar foils. All the wire planes have 2 mm wire spacing, and the single plane efficiency is $\approx 95\%$.

The drift chambers have four wire planes with wire configuration chosen to reduce the ambiguities in point reconstruction. The single plane precision varies with drift distance from 300 μm to about 500 μm near the field wires, and the single plane efficiency is 90% . Further details of the wire and drift chambers are found in tables 1 − 3 and in ref. [3].

The magnets for momentum analysis, M1 2.7 m downstream of LEBC and M2 18 m further downstream [1], have the main field axis in the Z−direction (horizontal). Positively charged particles were bent upwards in the first half of the proton run, and downwards in the second half.

M1 is a Helmholtz type magnet with two superconducting circular coils mounted on square iron plates held apart by four cylindrical bars. The distance between the coils is 82 cm and their inner and outer diameter are 150 and 210 cm respectively. The current was typically 1000 A, giving a field at the centre of 0.8 T and a 480 MeV/c vertical momentum kick.

The magnet M2 is a conventional C−type magnet with aperture 50×100 cm^2. The gap was increased for this set−up in order to match the acceptance of the detectors. The field obtained for 500 A results in a vertical transverse momentum kick of 450 MeV/c.

Field maps are computed with the program TOSCA, using a finite element method to solve the partial differential equations derived from Maxwells equations for the system [13]. The solution for each magnet is given as three−dimensional field components on a cubic lattice with dimensions:

− M1	$0 < x < 695$	$0 < y < 100$	$0 < z < 60$
− M2	$0 < x < 200$	$-55 < y < 55$	$0 < z < 25$

The final map consists of field values in about 5000 points such that linear interpolation between any two adjacent points on a main axis gives less than 1% residual from the intermediate values of the complete solution. The central M1 field values agree to within 22 G (better than 0.62%) with measurements using nuclear magnetic resonance. We normalize the field by making the computed K^0 mass agree with the accepted value (sect. 3.6). The M2 field was shifted by 1% to give particles traversing both magnets identical momentum measurements.

The magnetic fringe field in M1 is appreciable outside the lattice volume of the computation, where the field is approximated with the usual analytic form for a double dipole.

2.6 Charged particle identification

This section describes four detectors which make use of different techniques to provide charged particle identification in the entire momentum range. The overall performance of the system is given in sect. 4.

(a) The Silica Aerogel Detector (SAD)

SAD is a Cerenkov detector using Silica aerogel as radiator [14]. It is situated 5 m downstream of LEBC in the fringe field of the magnet M1. Two identical square sections, separated by a 70 cm gap to let forward particles through, cover an area of 115×294 cm^2. Fig. 6 displays the cell structure and the iron shieldings for the photomultipliers. The material within the acceptance represents 1.8% of an interaction length and 5.6% of a radiation length, mainly due to the aerogel.

The refractive index of the aerogel is 1.031, giving threshold momenta 0.56, 2.0 and 3.8 GeV/c for π, K and p respectively. Fig. 7 shows the number of photoelectrons as a function of momentum. The light yield for minimum ionizing particles decreased from 10.6 photoelectrons measured in tests in mid 1980 to 7.3 photoelectrons estimated from NA27 π^-p data collected at the end of 1982. The average light yield found in pp data (collected from the end of 1983 until mid 1984) is 5.5 photoelectrons. This decrease is believed to be explained by water from the air being absorbed by the aerogel.

23% of the reconstructed tracks with a hit in W2 have a hit also in SAD. The particle identification is unreliable for multiple tracks in the same module and single tracks close to the edge of a module. After elimination of these, 66% of the predicted tracks remain with good particle information.

(b) The Drift Chamber ISIS

ISIS (Identification of Secondaries by Ionization Sampling) is a drift chamber with a 40 m^3 fiducial volume. The construction and performance of a test module used in the NA16 Experiment is described in ref. [15], the performance of the complete detector in the π^- part of NA27 is described in ref. [16] and a summary follows here.

The fiducial volume is divided into two drift spaces by a single horizontal wire plane at half the chamber height about 15 cm above the the beam axis. Fig. 8 shows part of a vertical section parallel to the beam. A uniform 500 V/cm drift field is formed by aluminium tubes and gives the electrons a drift speed of 2 cm/μs. 640 anode wires connected in pairs to multihit electronics, give the X and Y$-$coordinates and dE/dx measurements of up to 320 points for each track. A maximum of 32 ionization measurements can be stored by each channel per event. The electronics and the pattern recognition program are monitored by including two electronically generated tracks in each data readout.

Straight tracks through the measured points are obtained with a filtering program and the ionization is obtained by comparing the measured pulse heights with a model dE/dx distribution. Typical ionization measurements are in the pion and proton runs based on 250 and 150 samples with FWHM of 8.3 and 11.9% respectively. The theoretical expectations on these numbers are reported in ref.[17]. An increased number of background tracks and low momentum tracks which traverse only a part of the chamber (sect. 3.4) are mainly responsible for the decrease of the number of ionization points. Tracks within 2 cm of the beam suffer in addition from a decrease of the ionization due to local space charge effects.

Given the momentum, a one degree of freedom χ^2 probability for each mass hypothesis is obtained from the fit of the observed ionization to the model distribution. The probability distribution is flat, as shown in fig. 9 for the pion hypothesis. Unambiguous particle identification is obtained when rejecting hypothesis with probability $< 1\%$. Defining separation by the requirement that $> 50\%$ of the particles are unambiguously identified, e/π separation is obtained in the momentum range $2-25$ GeV/c, π/K separation in the range $4-30$ GeV/c and K/p separation for momenta $7-40$ GeV/c [17].

(c) Forward Cherenkov detector (FC)

The 12 m long gas Cherenkov detector FC provides identification for particles in the second lever arm [18]. The refractive index can be varied by means of gas mixing (helium and nitrogen) and/or temperature control, giving threshold momenta for protons in the range $70-150$ GeV/c .

14 cells are arranged in a 2×7 matrix, each having a 28.6×52.0 cm^2 concave mirror with a radius of curvature of 2 m. The Cherenkov light is focused on photomultipliers (9761Q A EMI), and the signals are converted in linear 12 bit analog to digital converters (2249A LeCroy). Each photomultiplier is calibrated by means of light emitting diodes.

The refractive index of the gas is monitored by a refractometer using a He$-$Ne laser. A microprocessor computes corrections based on the gas mixture and pressure, the temperature in the chamber body and the refractometer reading. The chamber pressure is kept slightly above atmosphere to prevent contamination by air. Changes in the refractive index with normal temperature and pressure variations are both about 1% .

In NA27, helium at ambient temperature was used as radiator. The refractive index was typically $1+35\times10^{-6}$, giving thresholds for π/K/p of 17, 60 and 112 GeV/c respectively. The efficiency (fig. 10) is determined from the number of photoelectrons measured in one cell with unseparated proton beams in the momentum range $110-160$ GeV/c.

(d) Transition Radiation Detector (TRD)

Transition radiation is in EHS used for the first time to separate pions from kaons and protons at high momenta where other methods become inefficient.

TRD is situated between the drift chambers D5 and D6. It has twenty units of radiators combined with multiwire proportional chambers. The radiators are formed from a slurry of carbon fibres in water with a small amount of glue, dried in an oven and enclosed in mylar foil. The 7 μm diameter fibres have a density of 1.7 g/cm^3, and the bulk density of the radiators is 0.06 g/cm^3. The thickness vary from 110, 65, 55, 50, and 48 for the first five radiators to 45 mm for the following fifteen. Due to this variation, all chambers get an equal amount of transition radiation even though the radiation from one radiator is not fully absorbed in the following chamber. The total amount of material represented by the radiators corresponds to 14% of a radiation length, or 10% of an interaction length.

The MWPC have a transverse size of 100×200 cm^2 and a thickness of 4 cm. 96 sense wires, 20 μm in diameter, are stretched horizontally with 19 mm spacing, and three neighbouring wires are coupled to one preamplifier, resulting in a vertical resolution of 5.7 cm. The pulse heights are measured by $8-$bit analog to digital converters (ADC). The chambers are filled with a mixture of 19% xenon, 8% CH_4 and 73% He, having the same density as air. The 50 μm aluminized mylar windows function both as closure and cathode planes. The gas is circulated through a closed loop system, containing gas purifiers to remove oxygen and water vapour.

Energy calibration of TRD with electronically generated pulses, a radioactive Fe55 source and through going tracks results in correction factors for different wire chambers in the range 0.8 to 1.2 .

A significant separation between particles is obtained in the energy distribution from the 20 modules, fig. 11. The average deposited energy $<E>$, sampled over all chambers is shown in fig. 12 as a function of the Lorentz factor γ. The identification of charged particles with known momenta

improves with increasing γ, and the probability for correct pion identification increases from 90% at a momentum of 100 GeV/c to about 98% above 200 GeV/c.

For a 250 GeV/c K^+ enriched beam, the TRD measurement gives 12 ± 4% K^+, 48 ± 3% π^+ and 40 ± 3% protons, in good agreement with the beam composition of 10.3% K^+, 46.5% π^+ and 43.2% protons measured by the beam Cherenkov counters.

2.7 Calorimeters

(a) Electromagnetic calorimeters

Two lead glass calorimeters, the Intermediate Gamma Detector (IGD) and the Forward Gamma Detector (FGD) provide electromagnetic shower detection in lever arms one and two respectively. They have been described in detail in refs [3,19].

IGD is situated just behind the last drift chamber D3 in the first lever arm. It is made of 1139 lead glass blocks (15 radiation lengths) with 5× 5 cm^2 cross section, and has a 35× 85 cm^2 hole in the centre for the forward particles (fig. 13). The height of the hole was reduced by 5 cm for the final experiment in order to match the overall acceptance (the original design was optimized for a different distance to the target and beam momentum).

FGD is situated near the end of EHS and covers the image of the hole in IGD. It contains a lead glass converter wall (4.7 radiation lengths), a scintillator hodoscope with three planes of 1.5 cm wide fingers to measure the shower position and an absorber wall of 112 lead glass blocks (24 radiation lengths).

The monitoring procedure using a laser and the energy calibration with identified 50 GeV/c electrons are described in ref. [19]. The energy resolutions found from π^-p data are $dE/E = 0.15/\sqrt{(E)} + 0.02$ in IGD and $dE/E = 0.10/\sqrt{(E)} + 0.02$ in FGD (E given in GeV). The two shower separation distance is about 3 mm in both detectors, resulting in a FWHM of 20 MeV/c^2 for the π^0 mass peak in the $M(\gamma\gamma)$ distribution (fig. 14).

(b) Neutral hadron calorimeters

Both lever arms of EHS end with iron−scintillator calorimeters. Mounted behind the corresponding electromagnetic calorimeters, they offer good acceptance in the forward hemisphere for the neutral hadrons produced in strong interactions or originating from decays of charm particles. With this arrangement, the gamma detectors may be used as a part of the calorimeters for hadronic showers initiated in the gamma detectors.

The layout of the Intermediate Neutral Calorimeter (INC) is seen in fig. 15. The detector is composed of 24 cells, arranged to leave a 40×100 cm^2 hole that matches the acceptance of the second lever arm. The transverse size of the cells are 41×16 cm^2 on the sides and 16×33 cm^2 on top and bottom. Each cell is made of 12 massive, 5 cm thick iron plates, interleaved with 2 cm plastic scintillators. The iron corresponds to 3.6 interaction lengths, and the lead in IGD adds another two interaction lengths. The light from two scintillators is extracted laterally and seen by one photomultiplier. The whole detector is mounted on a support which allows horizontal and vertical movements.

Normally, 60% of the hadronic showers are initiated in IGD. Calibration data show that 95% of the INC signal is contained in the hit cell and the adjacent four cells. The total energy is written

$$E = (E_{NC} + E_{GD}) \times f(E,r) ,$$

where $r = E_{GD} / (E_{GD} + E_{NC})$ is the energy partition. f(E,r) is a polynomial of second degree in both E and r whose coefficients are fitted from calibration data. A fit to the three energy points (40, 60 and 80 GeV), gives an energy resolution of $\sigma(E) = 1.5\times\sqrt{(E)}$ with E in GeV (fig. 16).

Using the centre of gravity for the shower, the space resolution (RMS) in INC alone is about 15 cm. From the observation that 9% of the charged showers are associated with two tracks, the loss of neutral tracks is estimated at 6% . Comparison of neutral showers in INC alone and INC + IGD shows a considerable background of low energy showers. A cut at 3 GeV is therefore applied, removing 16% of the good neutral showers, as estimated by Monte Carlo simulation.

The Forward Neutral Calorimeter (FNC) is designed to detect and absorb 95% of the shower of hadrons with energies from a few GeV up to 400 GeV. This is achieved with 80 cm iron and the lead in the FGD, corresponding to 4.8 and 1 interaction lengths respectively.

The detector has 10×20 cells covering a total area of 150×300 cm^2. 16 iron plates, $15\times15\times5$ cm^3, separated by 2 cm thick plexipop scintillator form a cell of 114 cm length (fig. 17).

The light is collected by longitudinal rods of wavelength−shifter (Roehm plexiglass GS 218 doped with BBQ). The rods go through holes in the scintillator and iron plates, having a diameter of 20 mm to match the size of the photocathode. Each cell has a photomultiplier (FEU−84), matched to the spectrum emitted by the wavelength shifters and coupled to a LeCroy 2282 ADC.

Every cell of the calorimeter is calibrated with a muon beam for the electronic response and the absolute energy calibration is obtained with π^+ and proton beams at five energies: 40, 115, 160, 250 and 400 GeV. Fig. 18 shows the reduced variable $(E_{calorimeter} - E_{spectrometer})/E_{spectrometer}$, which has a mean value of -0.0012 (mean residual bias). The energy resolution is given by $\sigma(E) = 1.21\times\sqrt{(E)}$, where E is in GeV (fig. 16).

The lateral extension for 99% containment of showers in FNC alone (calibration data) is about seven cell widths. The space resolution is given by $\sigma(E) = 22.5/\sqrt{(E)}$ cm, and is partly consequence of the fact that 80% of the showers are initiated in FGD and the showers become wider between FGD and FNC.

Off−line reconstruction of a shower is done in an iterative way. A cell with the highest local energy is assumed to be the centre of the shower, and energy in surrounding cells is attributed to the shower or shared with a new shower, depending on the energies in the neighbouring cells.

FNC was hit by 1.8 charged particles per event on the average, 0.4 of them not coming from LEBC. Out of 3.1 neutral showers, 2.2 belong to low energy background or have an origin outside LEBC. 7% of the showers associated with several charged hadrons cannot be separated, and bad energy partition is observed in 4% of the cases with separated showers.

2.8 The Trigger

The trigger used in NA27 was designed to meet four basic demands:

- ensure that the beam particle is well in focus of the cameras,
- provide precise timing for the bubble chamber and the spectrometer,
- select inelastic interactions with minimum bias,
- reject interactions in the bubble chamber windows.

The first two demands are met with the use of a set of scintillators (T1 − T4, V1 − V2). These are seen in fig. 4, and table 9 gives the dimensions and position upstream of LEBC. In ordinary data taking, the hits in the trigger chambers SSD0, SSD1, W0 and W1 are recorded in latch registers after a beam trigger, defined by the coincidence $T1 \times T2 \times T3 \times T4 \times \text{not}(V1 + V2)$.

Inelastic interactions are selected by a multiplicity trigger demanding more than two hits in W0 and W1. On this trigger level, readout or analog − to − digital conversion of all detectors is initiated. The complete event information is read to the computer unless there is a veto from the fiducial volume trigger (FVT) within 8 μs. The laser for the bubble chamber illumination is fired 70 μs after a beam trigger and the readout is completed 60 ms later. A more detailed description of the trigger system is found in ref. [9].

Interactions occur equally frequent in the bubble chamber windows as in the hydrogen, and the FVT was designed to reject events with window interactions. The trigger logic checks in the horizontal projection whether the hit patterns in W0, W1, SSD0 and SSD1 are compatible with an interaction in one of the two bubble chamber windows. The procedure is illustrated in fig. 19. Assuming that the interaction has taken place in a window, the hits in W1 are predicted from the hits in W0 and the intersection of the beam particle with the window as measured by the silicon strip detectors. A single hit in each of the silicon detectors is required for a veto. The predictions are compared with the actual hits and a status bit is set for each window according to the number of matches and mismatches in the comparison. The 'exclusive − or' of the two bits is used in the trigger system to reject the event. The central 16 wires in W0 are excluded from the algorithm as the uncertainty in the X − position becomes large for small angle tracks.

From a subset of the data, the trigger efficiency (the triggered fraction of the total inelastic cross section) is found to be 80.3 ± 4.5%, in agreement with the value found for the full π^- sample. The trigger efficiency for charm events is estimated at 98^{+2}_{-3}%.

A comparison of the measured charged multiplicity distribution with published data at the same energy [20], reveals a trigger inefficiency for low multiplicities, fig. 20. A Monte Carlo simulation of the trigger has shown that this bias is of little importance for the trigger efficiency in charm events due to the high mean decay multiplicity of charm particles. A serious loss of events could occur only for very forwardly ($x_F > 0.8$) produced charm particles, which are triggered with an efficiency of about 50% .

The performance of the FVT is estimated from a sample of 1451 unbiased triggers and the recorded information from the FVT. The distribution of the interaction point for events vetoed by the FVT is peaked at the position of the bubble chamber windows, as expected. It also shows that some events in hydrogen, estimated at 7.6 ± 1.1%, are rejected. The FVT increases the probability for a picture to contain an interaction in the fiducial volume from 47.4 ± 1.8% to 59.5 ± 2.4% , but the rate of good primary interactions is unchanged due to the dead time following a veto.

The basic layout of the trigger was the same for all EHS experiments although differences did exist. Different running modes, such as calibration and data taking, caused small changes in the logic of the trigger system and motivated the use of programmable logic units for some of the functions. The state of six output signals as function of up to eight input signals are preprogrammed and tested, allowing fast redefinition of the logic and reducing the risk of unintentially removing or changing signals in the trigger.

2.9 Data Acquisition and online monitoring

The Data Acquisition System (DAS) is extended from a CERN standard package for Nord computers [21], employing circular buffering of data between producer tasks reading from CAMAC, and consumer tasks doing output on tape or online analysis. This system allows several detector subsystems to simultaneously perform checks and calibrations on real or simulated data as soon as the computer is relieved from higher priority tasks.

The main changes from the system reported in ref. [3] are:

- the main computer is a Nord ND100,
- for monitoring of the trigger system, a 16 channel Logic Analyser is introduced,
- programmable logic units are used for several functions.

The computer memory buffer is 64K 16−bit words, and a typical event requires 12K words. Normally the computer does not slow down the datataking rate as the data transfer speeds between CAMAC−computer and computer−tape drive are equal (2.5 μs/word). An exception occurs when a subsystem is doing tests on a big fraction of real events. The readout time matches the maximum event rate set by the cameras (15 Hz).

Besides the monitoring of several detector systems by a Nord ND10S as described in ref. [3], a logic analyzer was used in the main trigger to monitor the timing and the order of all trigger signals. This device displays the state of up to 16 chosen signals in a wide range of time delays and resolutions, and allows efficient error traceback in cases of trigger malfunction. The signals and logical functions of the programmable logic units in the trigger could be checked on−line with a program running on the main computer.

3 Event reconstruction

The event reconstruction starts with visual scanning of the vast amount of pictures for charm candidates and is followed by a first measurement of these. A standardized data structure containing the bubble chamber measurements and the electronic data is setup for the selected events, and these are processed through the program chain for geometrical reconstruction, particle identification analysis and kinematical fitting.

3.1 Scannning and measuring

The scanning procedure is common to all the participating laboratories. In the first scan, every picture is scanned by operators in two views and with two magnifications (10× and 30×). A prediction for the position of the interacting beam track is obtained from the upstream wire chambers. When an interaction is found, a 4 mm wide scanning box centred around the beam is searched for decays and secondary interactions. A second scan is made on frames with an interaction found in the first scan. A third scan is made by a physicist on events containing secondary activity in the scan box, or when the first two scans give different results.

The efficiency to find an interaction is very close to one, whereas the double scan efficiency to find secondary activities depends on the event topology. For events with neutral strange decays or charged secondary interactions the efficiency is 98%, and with charged strange (one−prong) decays it is 90% .

In charm events, tracks and vertices are often obscured in the forward cone of particles from the primary interaction, but the decays may still be resolved due to significant impact parameters and constraints in the number of tracks. We estimate the finding efficiency to vary between 85 and 95% , depending on the cuts applied (different cuts are used for different physics). After the first measurement and geometry processing, events are kept if :

i) the decay is inside a cylinder with radius R, centred around the incident beam particle (the charm box),

ii) the decay length is less than L,

iii) the number of tracks from the decay, outside a spectrometer acceptance of 180 mrad is less than N, and

iv) all impact parameters are less than T.

The values of these parameters depend on the topology, and are given in table 10. The cuts reject most of the strange particle background and a small fraction of the charm particles, less than 10% in the C1 and V2 topologies and practically nothing in any other topology(†). Decays giving fits to strange particles in a kinematic analysis are removed from the sample and the remaining charm candidates are remeasured on a single measuring machine HPD and reprocessed through the whole reconstruction chain.

The HPD is a High Precision measuring Device, which automatically digitizes the bubble positions [22]. Interactive graphical treatment of the HPD digitizations provides accurate vertex determination, correct association of tracks and vertices and therefore very good assignment of decay topologies. The RMS of the residuals to a straight line fit is 1.8 μm with an average track length in the bubble chamber of 5 cm and about 25 master points. After reconstruction of a primary vertex, the er-

(†) The decay topologies are designated after the connecting track and the multiplicity. C for charged connector, V for neutral and X for an ambiguous connector. Eg, C3 means a charged particle decaying into three charged secondaries.

ror on the impact parameters to that vertex is measured at 2.5 μm which enables detection of impact parameters with very high efficiency down to 7 μm. 15% of the decays were not found at the scanning level, but were later found by the HPD measurements. Fig. 21 shows the digitizations for the event in fig. 3, and illustrates how close tracks are separated by the magnification in the transverse direction.

The data reduction obtained with these procedures results in the following number of events :

- pictures from LEBC 2.3 million
- interactions in scanning 1.014 million
- events kept after first geometry 337
- events kept after HPD measurement 322

The 322 events contain 553 charm decay candidates, 231 pair decays and 91 single decays. 429 decays have charm signature and clear topology, 52 decays have a charm signature but ambiguous topology and 72 decays have no charm signature but appear with a charm decay in the same event. The clear charm decays are distributed into 64 C1, 134 C3, 7 C5, 169 V2, 53 V4 and 2 V6. Various number of these decays are used in the analysis depending on the physics.

3.2 Spectrometer alignment

Approximate position and orientation of all detectors in a common coordinate system are determined from measurements of external reference points on the detectors and the information supplied by the designers. Precise data are obtained by reconstructing a large number of non−interacting beam tracks (transverse position) and secondary tracks (the inclination of chambers and position along the beam). The chamber constants were found to be stable during each running period, and fluctuations due to temperature and pressure variations etc were less than 10% of the single track residuals (< 30 μm).

The angular precision of tracks is limited by the precision in the measurement of fiducial marks to ≈ 0.1 mrad in φ and 0.3 mrad in λ. φ is the projected angle in the XY plane (the bending plane which is parallel to the film plane), and λ is the angle to this plane. Alignment of the bubble chamber to the spectrometer is performed for each charm event with reconstructed non−interacting beam tracks, recorded in the same picture before and after the event.

3.3 Geometrical reconstruction

The track reconstruction philosophy is very different in NA27 compared to NA16. Due to a considerable number of background hits and ambiguities in the drift chambers, pattern recognition in NA27 relies on bubble chamber track images, on the proportional wire chambers in the zeroth lever arm, and the two−dimensional (XY) track segments provided by ISIS. The steps in the reconstruction procedure are :

i) setup a list of track candidates in the XZ−plane (non−bending) through the vertex and the hits in W0/W1,

ii) combine the ISIS track segments in the XY−plane with these candidates, and look for hits in W2 at the intersection,

iii) assign hits in the wire planes (multiplets) in W2 to the space tracks obtained from linking the bubble chamber tracks with ISIS tracks,

iv) confirm the tracks and resolve ambiguities with the hits in the drift chambers,

v) construct space tracks from remaining tracks in the bubble chamber and unused hits in PIC and W2. Confirm these in the drift chambers,

vi) Construct neutral decays in the spectrometer from remaining ISIS tracks and unused drift chamber hits.

In step i), all combinations of the two bubble chamber track images are tried together with all hits in W0/W1. The predictions in W2 are contained in a horizontal band (†), which is at best precise to 3 mm (multiple scattering and minor magnetic components increase this number).

The track candidates are subject to quality checks, based on the density of wire chamber hits and the track length and orientation in ISIS. With up to 320 points available, ISIS track finding is very efficient but a few percent of the tracks are unresolved due to confusion in the forward region and an appreciable background from out−of−time beam tracks. About 90% of the reconstructed tracks have

---

(†) In general, a cluster of hits in the wire chambers is treated as a single hit with enlarged error. However, in W0/W1 the hits are treated individually since the most frequent cause of clustering is several tracks being too close to be resolved.

ISIS track segments and the remaining 10% (found in step v) are mainly low momentum tracks outside the ISIS acceptance. These latter tracks include tracks with secondary interactions upstream of ISIS (usually in SAD or the ISIS entrance window) and some high momentum tracks improperly resolved by ISIS.

All bubble chamber tracks have their space direction reconstructed (where necessary track images are matched by manual comparison of bubble patterns). 70% of all tracks and almost 100% of those with $x_F > 0$ are inside the M1 acceptance. From a study of kinematically fitted strange particles and from the symmetry of pp interactions, the efficiency for linking bubble chamber tracks into the spectrometer is found to be 96% for tracks with $x_F > 0$.

Some of the ISIS tracks which are not associated to any bubble chamber track, originate from decays outside the bubble chamber. A dedicated routine performs kinematical fitting to all vertices of those pairs of tracks that fulfill simple geometrical constraints. The efficiency to reconstruct a neutral decay outside the bubble chamber is governed mainly by the probability for the geometry program to find the decay products, i.e. mainly by the acceptance of ISIS. This was confirmed by using strange particle decays, reconstructed without making use of the bubble chamber information.

Fig. 22 shows the momentum distribution for reconstructed tracks entering the first and second lever arms respectively. We notice that secondaries from charm decays have roughly the same distribution as the primarily produced particles.

The γ and π^0 reconstruction from showers in the electromagnetic calorimeters are described in some detail in ref. [3]. The shower recognition starts in IGD with the light collected in the lead glass blocks and in FGD with the light in the scintillator hodoscopes, taking the counters with highest amplitude as the centre of showers. A cut at 0.5 GeV (may vary with the physics) imposed on the shower energy reduces low energy background showers, but has little influence on the number of reconstructed π^0 due to the finite granularity of the detectors. The reconstruction efficiency is close to 100% for π^0 with momenta below 40 GeV/c, decreasing to zero at 100 GeV/c . In FGD, the efficiency is almost 100% for π^0 momenta between 30 and 300 GeV/c. The π^0 signal to background ratio is 1:2, fig. 14.

3.4 Acceptance

The φ angle of tracks from primary interactions extend above 400 mrad, as shown in fig. 23. The angles of reconstructed tracks are well below 200 mrad due to material in the zeroth lever arm. The losses in the central bins are caused by simultaneous large values of the λ angle.

For straight tracks, the acceptance into the first lever arm is limited as follows. The λ angle is restricted by the frame of PIC and the M1 coils to 100 mrad for $\varphi > 0$, decreasing to 90 mrad for tracks with $\varphi = -150$ mrad due to the inclination of PIC. This is seen in fig. 24 as a steep decrease at 100 mrad of the ratio between the number of reconstructed and measured tracks from primary interactions (the distribution of the interaction point along the beam is flat). The φ angle is restricted to about $\pm$ 120 mrad, mainly by the rectangular frame of W0 and the circular frame of MDC1.

In the second lever arm, the production angles of reconstructed tracks are limited to about $\pm$ 10 mrad in λ and to $\pm$ 25 mrad in φ by the hole of INC and the gap of M2 respectively. The tails in the φ distribution shown in fig. 25 are due to the deflection in the magnet M2 and decays and interactions far downstream of the bubble chamber. Table 11 summarizes the geometrical acceptance. The spread is due to the vertex position in the bubble chamber and given by the RMS of the observed angular distributions.

The effect of several combinations of magnetic fields in M1 and M2 on acceptance and momentum resolution (dp/p) was studied in a Monte Carlo simulation. The results are illustrated in fig. 26, showing the acceptance as a function of dp/p in SAD and for particles entering the second lever arm. A low field in M1 favours the identification of low or relatively low momentum particles in both SAD and ISIS, which are numerous also in charm decays (fig. 22). A low field in M1 also increases the acceptance into the second lever arm where the momentum resolution is improved and further identification is obtained from FC. The useful momentum range for particle identification in FC for different thresholds was estimated with Monte Carlo simulation, showing an optimum for the π threshold around 18 GeV/c.

Good values for the acceptance and momentum resolution are obtained for intermediate magnetic fields in M1 and M2 (giving p_T kicks $\approx$ 500 MeV/c), which also give small acceptance variations. The selected currents are given in sect. 2.5 .

The acceptance for charm particles in different decay modes is estimated by Monte Carlo simulation. The model includes the experimentally found production characteristica in the form

$$d^2\sigma/dx_F dp_T^2 = A \times (1-x_F)^5 \times \exp(-1.1 \times p_T^2)$$

and the spectrometer acceptance presented above. Fig. 27 shows the result for two decay modes of D^0 produced in 400 GeV/c pp interactions. Around $x_F = 0$ there is a rapid increase in the acceptance from zero to the maximum value. The lower reconstruction efficiency for π^0 compared to charged particles is apparent from the acceptance curve for fully reconstructed D^0 with one seen π^0, broken line. The acceptance for three and four−prong decays with all tracks reconstructed is practically the same.

3.5 Momentum measurement

The track angle precision in the bending plane is typically 0.1 mrad in LEBC and 0.03 and 0.02 mrad in the two lever arms respectively. Material corresponding to 4% of a radiation length between LEBC and the first lever arm gives an additional angle error due to multiple scattering with an RMS of 3/p mrad (p in GeV/c). For momentum measurement this should be compared with the angular deflection from M1 of at least 480/p mrad. The magnetic field uncertainty corresponds to a momentum error of 0.04% after calibration at the K^0 mass (see sect.s 2.5 and 3.6). The momentum resolution is thus dominated by the multiple scattering, and is at best 0.5% . Fig. 28 shows the measured dp/p for tracks traversing different parts of the spectrometer. The average momentum error of 0.8% is practically independent of the momentum due to the extra measurements from the downstream chambers and the M2 magnet.

3.6 Mass resolution

The experimental mass resolution is determined from the invariant mass of all reconstructed two−prong decays in the charm box (1183). The $\pi^+\pi^-$ combinations in the K^0 region are shown in fig. 29a. The peak has a FWHM of 7 MeV/c^2 and similar peaks for the $p\pi^-$ and $\bar{p}\pi^+$ combinations in the Λ^0 region have FWHM of 2 MeV/c^2, figs 29b and 29c. The K^0 mass was used to determine the absolute calibration of the M1 magnet, thus reducing the systematic error in other mass regions to the propagated statistical K^0 mass error (0.2 MeV/c^2 from 420 decays).

Before computing masses, we remove the background with the following requirements:

- both tracks well reconstructed,
- transverse momentum balance to select two-body decays,
- maximum transverse momentum less than 250 MeV/c to remove the charm background,
- opening angle in the bending plane greater than 5 mrad, and
- e^+e^- invariant mass greater than 30 MeV/c^2 to reject γ conversions.

We further exclude, for the $\pi^+\pi^-$ invariant mass, those combinations for which the $p\pi^-$ and $p\pi^+$ assignments are within 20 MeV/c^2 of the Λ^0 mass, and similarly for the $p\pi^-$ and $\bar{p}\pi^+$ invariant masses. We obtain 1115.5 $\pm$ 0.2 $\pm$ 0.1 MeV/c^2 for the Λ^0 (172 decays) mass, in good agreement with the published value of 1115.60 $\pm$ 0.05 MeV/c^2 [23]. The mass resolutions are 3.0 and 0.9 MeV/c^2 for K^0 and Λ^0 respectively, in agreement with the values expected from the momentum and angle errors. The correctness of these errors was verified by kinematic fit probabilities and the pulls on measured momenta and angles.

The mass resolution in the D-region varies with the decay mode. From the invariant mass of two and four-prong charm decays (fig. 30), we obtain a mass resolution of 11 MeV/c^2 for $D^0 \rightarrow$ all charged particles. Only Cabibbo favoured combinations compatible with particle identification have been considered. We note a reflection around 1500 MeV/c^2 from incorrect mass assignments and from decays with neutral particles. The mass resolution for decay modes with seen π^0 extends up to 40 MeV/c^2. From 19 fully reconstructed D^0 without neutral decay products, we obtain a mass of 1865.1 $\pm$ 1.8 $\pm$ 0.8 MeV/c^2. The analysis of the charged charm particle mass resolution is complicated by the presence of $D^{\pm}$, D_s and Λ_c which kinematically reflect into each other.

4 Particle identification

Charged particle identification in the first lever arm (momenta mainly below 30 GeV/c, fig. 22) is obtained with the Cherenkov detector SAD and ionization sampling detector ISIS. Electrons, π^0 and γ are detected by the lead glass calorimeter IGD, and neutral hadrons by the iron calorimeter INC.

Another combination of detectors, FC, TRD, FGD and FNC provides additional charged and neutral particle identification for the particles entering the second lever arm of the spectrometer.

The particle identification is studied with a sample of 3996 tracks. 3892 of these have some particle identification information, 800 come from a charm vertex and 700 have no connection with a bubble chamber vertex (hanging track). The mass selection is based on the following main rules (†).

ISIS	For tracks with $\geq$ 100 ionization measurements, mass hypotheses are accepted if the probability is > 4%, for tracks with < 100 ionization measurements the probability cut is 1%,
SAD	A mass hypothesis is vetoed if the momentum is below threshold and there is, a signal corresponding to > 0.5 photoelectrons,
FC	If several hypotheses are allowed, only those with probability > 5% are accepted,
TRD	Mass hypotheses are accepted when the probability is > 5%
Calorimeters	Hypothesis with probability < 0.1% are vetoed

For ISIS and TRD, the probability of a mass hypothesis is obtained from a fit of the energy deposition to a model distribution. In the other detectors, the probability is given by the signal (observed number of photoelectrons) and the number expected from Poisson statistics.

Table 12 gives the acceptance, a figure of merit and momentum range for the charged particle detectors. The acceptance is defined as the number of tracks with particle identification information, divided by the number of reconstructed tracks with a hit in W2 (3996) or D4 (856) (W2 is used for normalization for the detectors in the first lever arm and D4 for those in the second lever arm). The figure of merit is the number of tracks with reliable identification information divided by the number of tracks with a signal in the detector and the momentum range gives approximate limits for discrimination between different particles. The main causes for unreliable particle identification, apart from inherent limitations such as statistics, are:

- in the beam region of ISIS, local space charge accumulation changes the electric field and thereby the track information,

(†) A mass hypothesis may be vetoed, allowed or accepted. Accepted means that there is positive evidence for the considered mass.

– close to the edges of the cells in SAD and FC the light collection is inefficient,

– several particles traverse the same cell of SAD or FC, or are too close to be resolved in ISIS.

To check the consistency of particle identification among the detectors, the particle contents in samples of tracks from charm decays have been determined on a statistical basis using the maximum likelihood method on ISIS ionization information [24]. The results are compared with the IGD/FGD and FC information, and summarized in tables 13 and 14. Comparing the detectors on single track basis, the number of conflicts between unique hypothesis in ISIS and vetos from other detectors are below 1% for the tracks with reliable information.

81% of the tracks with good particle identification are found in ISIS. 37% of the good tracks are assigned a unique mass by ISIS alone, and 43% by the combination of all detectors (†). The fraction of tracks in ISIS with unique identification is shown in fig. 31 as a function of the momentum.

For 7% of the tracks with a momentum less than 10 GeV/c, reliable identification information is obtained from SAD but not from ISIS. TRD adds information for 26% of the tracks with $p > 70$ GeV/c where no other information is available. The calorimeters exclude electron hypothesis for 36%, muon hypothesis for 23 % and hadron hypothesis for 8% of all tracks with particle identification.

In the next section we give a few examples of how particle identification has been used in the reconstruction of charm decays.

(†) Pions and muons are practically identical from ionization point of view. In the ionization detectors, no distinction is therefore made between the two, but both the electromagnetic and hadronic calorimeters may identify muons.

5 Reconstructed charm events

We illustrate the event reconstruction and particle identification with six examples of reconstructed charm decays. A summary of particle identification data for these decays is given in table 15.

Decays 1 and 2

These decays belong to the event shown in fig. 3. It contains two neutral decays with two and four charged tracks respectively with all tracks successfully reconstructed. Both decays require neutral particles to balance transverse momentum, and the kinematic program leaves several ambiguities about the mass of the decay products, but some may be resolved.

The transverse momentum of one of the tracks in the V2 decay, 478 ± 56 MeV/c, makes a strange decay unlikely and charm decay most probable. Semi−electronic and multineutral solutions are obtained for the V2, but none is accepted for physics since the electron is not uniquely identified and the other solutions demand several neutral particles.

Using the absence of signals in the calorimeters (at the proper position), the charm quantum number determined by the K^+ in the V2 decay, and excluding Cabibbo unfavoured, non−constrained solutions, a single hypothesis remains for the V4 decay which uses the 14 GeV/c track for the K^- . The decay mode is $D^0 \rightarrow K^-\pi^+\pi^+\pi^-\pi^0$, having a x_F of 0.11 and a proper time of 5.5×10^{-13} s.

Decay 3

This is a C1 decay which obtains a 3−constraints fit with the use of neutral particles observed in the calorimeters. The single charged track with momentum 3.7 GeV/c is assigned K or proton masses by ISIS, but a signal of 4.2 photoelectrons in SAD rejects the proton hypothesis. With a neutral K and a π^0 observed in INC and IGD respectively, a good fit to the (Cabbibbo unfavoured) decay $D^+ \rightarrow K^+K^0\pi^0$ is obtained with $x_F = -0.08$ and proper time $= 8.8\times 10^{-13}$ s .

Decay 4

A uniquely identified proton in ISIS together with a π^0 observed in IGD and a K^0 observed in INC, give a Λ_c in the decay mode $\Lambda_c \rightarrow p\pi^+\pi^-\pi^0K^0$. The x_F is 0.55 and the proper time is 0.50×10^{-13} s. Another two fits with other combinations of seen neutrals have x_F of 0.45 and 0.60 respectively.

Decay 5

Two tracks in this C3 decay are uniquely identified as μ and K, which leads to non−constrained solutions $D^+ \rightarrow K^-\pi^+\mu+(\nu)$. Two solutions are obtained, one with a slow and one with a fast neutrino.

Decay 6

In the last example, a unique identification of an electron is obtained by FC. Several close tracks in ISIS spoil the identification in ISIS for the 13.7 GeV/c track, but a clear signal in FC excludes the μ,π,K and p hypothesis. The decay mode is ambiguous as several solutions are obtained for various combinations of seen and unseen neutrals.

As these examples show, completely unique solutions for the decays are not always obtained. Very often the charm particles are identified, even though different π^0 can be used in the kinematical fits. The production variables have in general been found to differ very little between such solutions.

With the apparatus and procedures described here we have collected data that allow us to extract results on the following items:

- Λ_c lifetime and production properties,
- D^0 and $D^{\pm}$ lifetimes and production properties,
- correlation properties between hadrons produced in charm events and
- decay branching ratios of charm particles.

Besides the results from 400 GeV/c pp interactions, we have already published similar results from 360 GeV/c π^-p interactions [3].

It is worth noting that the performance attained with EHS corresponds well with that described in the initial proposals [1], presented ten years ago.

6 Summary

Results obtained by the LEBC−EHS Collaboration have been used to describe the set−up and performance of the final version of the European Hybrid Spectrometer (EHS), used to study charm particle physics.

With a rapid cycling, high resolution bubble chamber LEBC, a sensitivity of 38.3 events/μb in 400 GeV/c pp interactions was achieved. Bubbles with 17 μm diameter allow good track separation, and a measurement precision of 2.5 μm allows impact parameters down to 7 μm to be determined. Vertices of short lived particles, such as charm particles, are observed directly in the bubble chamber with an efficiency up to 90% for $D^{\pm}$, depending on the decay topology.

The bubble chamber was combined with a downstream spectrometer with large geometrical acceptance for reconstruction and identification of tracks. The overall acceptance is 70%, and tracks within the acceptance are reconstructed with an efficiency of 96% . Two lever arms with 0.3 and 0.2 mrad angular precision give a multiple scattering dominated momentum resolution $dp/p \cong 0.8\%$ in the major part of the momentum range, and a mass resolution of 3 MeV/c^2 is obtained for K^0. For D−mesons the mass resolution depends on decay mode and ranges from 11 MeV/c^2 for D^0 to $\approx$ 40 MeV/c^2 for decays containing neutral particles.

Several detectors cooperate to give identification for both charged and neutral particles over practically the full momentum range. 84% of the charged particles which are not swept away by the M1 magnet, have reliable identification information, and 43% are assigned a unique mass hypothesis.

This complex apparatus has proved very useful in several experiments. LEBC−EHS is a good example of a successful combination of the bubble chamber and electronic detector techniques for the direct observation and study of charm particles.

Its weakness is the limitation imposed on the sensitivity of such experiments, but its strength lies clearly in the limitation of systematic errors which affect experiments with more restricted triggers, acceptance or particle identification power. The fact that systematic errors are practically negligible with a set−up like LEBC−EHS, has resulted in one of the first reliable determinations of fundamental

quantities in charm physics, like the lifetimes of the D^0 and $D^{\pm}$ mesons and the charm cross section in hadronic production [25].

Acknowledgements

The conception, design, construction and running-in of a complex set-up like EHS could not be achieved without the effort of a large number of technicians, engineers and physicists, in particular from the teams of the CERN DD Division lead by David Jacob and of the EF Division, led by Dietrich Gusewell.

We also would like to acknowledge the essential help with all questions related to the beam and the accelerator, provided by Niels Doble and his collaborators.

Financial assistance by various national funding agencies is gratefully acknowledged.

References

[1] W.Allison et al., CERN/SPSC 75−15;
W.Allison et al., CERN/SPSC 76−43;
W.Allison et al., CERN/SPSC 77−44;
W.Allison et al., CERN/SPSC 78−91.
[2] CERN/SPSC 79−80/P129 and ref.s therein.
[3] M.Aguilar−Benitez et al., Nucl.Instr. and Meth. 205 (1983)79.
[4] LEBC−EHS Collab. M.Aguilar−Benitez et al., Z.Phys C31 (1986) 491−511.
[5] CERN/SPSC 80−51/P144.
[6] RCBC−EHS Collab. J.L.Bailly et al., Z.Phys C23 (1985) 205.
[7] P.Coet,N.Doble and S.Reucroft CERN/SPS/81−25.
[8] H.van Brungel and N.Siegel CERN/SPS 81−13.
[9] R.Bizzarri et al., Nucl.Instr. and Meth. 222 (1984) 441;
R.Bizzarri et al., USIP Report 85−10, University of Stockholm.
[10] J.L.Benichou et al., Nucl.Instr. and Meth. 190 (1981) 487.
[11] E.R.Belau et al., Nucl.Instr. and Meth. 192 (1982) 217.
[12] A.Bettini,D.Pascoli and M.Pernicka , Nucl.Instr. and Meth. 204 (1982) 65.
[13] A.Armstrong, TOSCA User Guide, RL 81−070 (1981), Rutherford Lab
[14] C.Fernandez et al., Nucl.Instr. and Meth. 225 (1984) 313.
[15] W.Allison et al., Nucl.Instr. and Meth. 163 (1979)331.
[16] W.Allison et al., Nucl.Instr. and Meth. 224 (1984) 396.
[17] W.Allison and J.H.Cobb, Ann.Rev.Nucl.Part.Sci. 30 (1980)253.
[18] F.Diez−Hedo, Proc. of the 13th int. winter meeting on
fundamental physics, Cuenca, Spain (April 1985) 1.
[19] B.Powell et al., Nucl.Instr. and Meth. 198 (1982) 217.
[20] C.Bromberg et al., Phys.Rev.Let 31 (1973) 1563.
[21] P.Bahler et al., Computer Physics Comm. 22 (1981) 285−292.
[22] J.R.Lutz and A.Michalon, II Vezelay Workshop on EHS, CERN/EP−EHS 80−2,
[23] Particle Data Group, Physics Letters 170B (1986) 1.
[24] LEBC−EHS Collab., M.Aguilar−Benitez et al., Phys.Lett. 168B (1986) 170.
[25] LEBC−EHS Collab., M.Aguilar−Benitez et al., Phys.Lett. 146B (1984) 266;
LEBC−EHS Collab., M.Aguilar−Benitez et al., Phys.Lett. 161B (1985) 400;
LEBC−EHS Collab., M.Aguilar−Benitez et al., Phys.Lett. 164B (1985) 404.

Table captions

Table 1 Position and size of all detectors in EHS.
The position is given relative LEBC, and refers to the centre of the detector. The sensitive area is given as width×height (ZxY) and thickness (length) is along the beam.

Table 2 Wire chamber data.
The orientation of wires in tables 2 and 3 is given in ° with respect to an axis in the XY−plane, i.e. the vertical for all chambers except the proportional inclined chambers. The pitch gives the distance between sense wires.

Table 3 Drift chamber data.

Table 4 Calorimeter data.

Table 5 Cherenkov counter data.

Table 6 Silicon strip detector operating conditions.

Table 7 LEBC operating parameters.

Table 8 MWPC operating conditions.

Table 9 Scintillator data. All numbers are given in cm.

Table 10 Measurement selection criteria.
The decay topologies are defined in sect. 3.1

Table 11 Geometrical acceptance fin mrad for straight tracks.

Table 12 Particle identification performance.

Table 13 ISIS − Gamma detector comparison.

Table 14 ISIS − FC comparison.

Table 15 Particle identification summary for the decays described in sect. 5.

Table 1

	Position(m)	Sensitive area(cm^2)	Thickness(cm)	
U1	−27.29	26 x 36	12	
U2	−16.25	same		(a)
U3	− 2.21	same		
SSD0	− 3.43	3 x 1	0.5	
SSD1	− 1.69	same		
LEBC	0.0	7 x 5	12	
W0	0.33	8 x 10	4	
MDC1	0.45	14 x 16	16	
W1	0.85	32 x 32	5	
MDC2	1.00	30 x 30	20	
PIC34	1.2	50 x 64	7	
PIC12	2.7	50 x 128	7	
M1	2.7	82	415	(b)
W2	4.28	120 x 215	20	
D1	6.86	210 x 430	20	
D2	14.53	same		
D3	15.55	same		
SAD	5.2	120 x 290	60	(c)
ISIS	10.7	200 x 400	512	(d)
IGD	15.0	200 x 180	42	(e)
INC	15.9	160 x 160	85	(f)
M2	18	50 x 100	180	(g)
D4	22.01	130 x 200	16	
D5	36.33	same		
D6	40.52	same		
FC	28	100 x 200	1200	
TRD	37	100 x 200	1080	
FGD	39	120 x 210	75	
FNC	42	150 x 300	114	

(a) U2 replaced U1 in the last part of the NA27 proton run
(b) this is the gap and length at the centre
(c) SAD has a 70 cm high gap centred around the beam
(d) the centre of ISIS is 15 cm above beam axis
(e) IGD has a 35 x 85 cm^2 hole
(g) INC has a 40 x100 cm^2 hole
(f) length of the pole gap

Table 2

	Nb. of planes	Orientation (°)	Pitch (mm)	HT (kV)	Efficiency (%)
U1	5	60,60,0,−60,−60(a)	2	4.9	99.5 (b)
U2	identical to U1				
U3	− " −	(c)			
W0	1	0 (vertical)	0.5	3.75	98.6
W1	1	0	1.0	5.4	99.5
W2	7	0,−90,60,80 −80,−60,90	2	4.5(c)	99.5
TRD	20(d)	90 (horizontal)	19		

(a) The ±60° planes are staggered two by two.
(b) The high voltage is controlled individually for each plane.
(c) U3 is identical to U1 but was mounted rotated 90° about the beam (X−axis).
(d) 20 modules with one plane each. Three wires with 19 mm pitch are connected to one preamplifier.

Table 3

	Nb. of planes	Orientation (°)	Pitch (mm)	Drift length(a) (mm)
MDC1	9	0 (vertical)	0.	8
MDC2	19	0	0.5	8
PIC12	2	−80,80(b)	2	8
PIC34	as PIC12			
D1	4	74,84,−84,−74	48/46	24
D2	identical to D1			
D3	− " −			
ISIS	1	90 (horizontal)	16(c)	2000
D4−D6	as D1−D3			

(a) The drift region of each wire is twice the value given.
(b) In the wire plane which is tilted 35 ° with respect to the vertical.
(c) Two wires with 16 mm pitch are connected to one preamplifier.

Table 4

	Nb. of cells	Material	Granularity (cmxcm)	Radiation/ interaction length
IGD	1139	lead glass	5 x 5	15
FGD converter	28	lead glass	60 x 15	5
hodoscope	375	plexipop	1.5 wide	–
absorber	112	lead glass	15 x 15	24
INC	24	iron/plexipop	41 x 16	4
FNC	200	iron/plexipop	15 x 15	5

Table 5

	Nb. of modules	radiator	cell size (cm x cm)	refractive index
SAD	18	aerogel	23 x 55	1.031
FC	14	helium	29 x 52	1.000035

Table 6

	SSD0	SSD1	
Bias voltage	+90	+90	V
Bias current	5	1.5	A
Efficiency	97.5	86	%
Cluster size(a)	1.03	1.04	
Signal/noise ratio	2	2	

(a) Cluster size gives the average number of adjacent fired wires per real hit

Table 7

Hydrogen temperature	29.0	K
Hydrogen static pressure	8.3	bar
Expansion pressure minimum	3.9	bar
Piston stroke	0.5	mm
Duration of expansion cycle	6	ms
Beam gate at pressure minimum	500	μs
Expansion cycling rate	30	Hz
Maximum camera cycling rate	15	Hz
Bubble density along tracks	80	cm^{-1}
Objective (diffraction limited up to f/5.6)	SERCO	
Focal length	288	mm
Demagnification	1:0.89	
Stereo angle	13	°
Nominal depth of field	1.5	mm
Bubble growth time(flash delay)	70	μs
Bubble diameter (two track resolution)	17	μm
Measuring prescision	2.5	μm

Table 8

	W0	W1	
Efficiency	98.6	99.5	%
Average cluster size(a);			
beam trigger	1.10	1.10	
interaction trigger	1.24	1.19	

(a) Cluster size gives the average number of adjacent fired wires per real hit

Table 9

	Width	Height	Thickness	Position
T1	10	25	0.6	3000
T2	10	25	0.6	290
T3	0.2	10	0.2	115
T4	10	3	0.5	271
V1	15	35	0.6	66
V2	15	35	0.6	66

Table 10

Topology	R(mm)	L(cm)	N	T(mm)
X1–X6	2.0	–	1	1.5
C1	0.6	–	0	1.5
V2	0.2	3	1	0.5
C3, V4, C5	2.0	–	–	–

Table 11

Detector	λ	φ
W0	100 – 140	100 – 140
MDC1	110 – 190	110 – 190
PIC	90 – 110	110
M1	100	no limit
INC/M2	11	25

Table 12

	SAD	ISIS	FC	TRD(a)	ALL
Acceptance					
all tracks	0.23	0.84	0.58	0.86	0.87
from charm	0.23	0.82	0.59	–	0.86
Figure of merit					
all tracks	0.66	0.78	0.75	0.68	0.97
from charm	0.70	0.80	0.80	–	0.96
Momentum range(GeV/c)	0.6 – 3.8	2 – 50	18 – 112	70 – 400	0.6 – 400

(a) For TRD the quoted numbers refer to tracks with $p > 70$ GeV/c, which make up 30% of all tracks in D4. Among the charm decay products, this fraction is only 12% and the statistics is very low (12 tracks).

Table 13

Gamma detector information		ISIS results electrons	pions	kaons	protons
hadrons	273	0.0	228.6	40.8	3.6
electrons	15	14.3	0.7	0.0	0.0

Table 14

FC vetoes		ISIS results electrons	pions	kaons	protons
electrons	29	0.2	7.7	21.1	0.0
pions	17	0.0	0.0	17.0	0.0
kaons	85	0.0	82.9	2.1	0.0
protons	101	0.0	99.8	1.2	0.0

Table 15

Decay	Topology	Momentum [GeV/c]	Selected hypotesis all	Selected hypotesis ISIS	Vetoed hypothesis SAD	Vetoed hypothesis GD	Vetoed hypothesis FC
1	V2	13.80	K	K	.	.	.
		– 1.92	–	–	–	.	.
2	V4	8.93	μ,π	μ,π	.	.	.
		– 16.47	μ,π,K	μ,π,K	.	e	.
		9.29	π,K	μ,π,K		e,μ	.
		– 14.35	μ,π,K	μ,π,K	.	.	.
3	C1	3.73	K	K,p	p	.	.
4	C3	25.26	π,K	π,K	.	–	.
		123.81	p	p	.	.	.
		– 26.55	μ,π	μ,π	.	.	.
5	C3	5.22	μ	e,μ	–	e	.
		11.08	no partid information at all				
		– 5.14	K	K	–	.	.
6	V2	– 2.48	e,μ,π,K	–	p	.	.
		13.72	e	–	.	.	μ,π,K,p

A particle name in the table means that the hypothesis is allowed (ISIS) or rejected (all other detectors). A hyphen means that there is information in the detector but no discrimination, and a dot means no information.

Figure captions

Fig. 1 Layout of the European Hybrid Spectrometer (see also fig. 4):

LEBC	Bubble chamber	SAD,FC	Cherenkov Counters
M1,M2	Spectrometer magnets	IGD,FGD	Lead glass calorimeters
U1 – U3,W2	Prop. wire chambers	INC,FNC	Iron hadron calorimeters
D1 – D6	Drift chambers	TRD	Transition radiation detector
ISIS	Ionization sampling drift chamber.		

Fig. 2 (a) the Lexan Bubble Chamber body.

The upper rectangular section contains the photographed volume (optical axis perpendicular to film plane) between the beam entrance window (left, 2 mm thick) and beam exit window (right, 3 mm thick). The circular section below houses the expansion membrane (29 cm diameter and 4 mm thick). The metallic parts on the top are from the left : filling valve, heat exchanger and pressure gauge.

(b) The bubble chamber mounted on its support cylinder.

The light square area is its optical window. The hydrogen reservoir and cold valves for chamber operation are visible above.

Fig. 3 LEBC picture with charm event, produced in a 400 GeV/c pp interaction.

Two neutral D – mesons decay at 5.1 and 7.1 mm from the primary vertex into four (V4) and two (V2) charged particles resp. (See also fig. 21). The straight beam track is used for alignment of bubble chamber and spectrometer.

Fig. 4 Schematic side view of the detectors close to the bubble chamber.

The veto counters V1 and V2 are seen from above:

T1 – T3,V1,V2	Scintillation counters,
SSD0,SSD1	Silicon strip detectors,
U3,W0,W1,W2	Proportional wire chambers,
MDC1,MDC2	Mini drift chambers,
PIC12,PIC34	Inclined proportional chambers.

Fig. 5 The multiwire proportional chamber W0 and the mini drift chamber MDC1. The common support can be moved into a position close to the exit window of the vacuum chamber to maximize the acceptance. Gas connections are seen on the vertical sides, and above is a box containing the preamplifiers for W0.

Fig. 6 Photo of the silica aerogel Cherenkov detector SAD showing the back of the reflectors and the iron boxes shielding the photomultipliers. The coils of the magnet M1 are seen in the centre.

Fig. 7 Average number of photoelectrons in SAD as a function of momentum. The numbers correspond to data collected in 1984.

Fig. 8 Vertical section of the ionization sampling detector ISIS parallel to the beam. Two sense wires are connected to one preamplifier. The mirror track, due to the up−down ambiguity, is initially considered a candidate in the reconstruction.

Fig. 9 ISIS ionization probability. The full histogram gives the pion probability for all tracks, the hatched gives the pion probability for tracks uniquely identified as pions (the criteria are given in the text).

Fig. 10 Efficiency of the gas Cherenkov counter FC. The proton curve is measured, the π and K curves are computed. The efficiency is given by the probability of having no signal for a real track (i.e. less than 0.2 photoelectrons).

Fig. 11 Distribution of the average deposited energy in twenty sampling units of the transition radiation detector TRD, obtained with a 200 GeV/c positive beam (a 10% K^+ contamination enter mainly into the pion distribution).

Fig. 12 The mean deposited energy as a function of the γ factor. Open circles give results without radiators, filled symbols with radiators: Circle 250 GeV/c π^+, square 250 GeV/c K^+ and triangles 80−200 GeV/c π^-.

Fig. 13 Photo of the lead glass calorimeter IGD in its support.

Fig. 14 Invariant mass distribution in the π^0 region for two − shower combinations. Cuts at 0.9 and 2.0 GeV are imposed on the shower energy in IGD and FGD respectively. The background curve is a Gaussian plus a polynomial of degree five.

Fig. 15 Photo showing the layout of the hadron calorimeter INC.

Fig. 16 Energy resolution of INC (circles) and FNC (crosses). The fitted curves are the expressions $\sigma(E) = 1.5\times\sqrt{(E)}$ for INC and $\sigma(E) = 1.2\times\sqrt{(E)}$ for FNC (E in GeV).

Fig. 17 Schematic structure of a cell in the hadron calorimeter FNC.

Fig. 18 The reduced energy $(E_{calorim} - E_{spectrom})/E_{spectrom}$ for charged tracks. The calorimeter energy includes the energy measured by FGD. The mean residue is 0.0012 and the FWHM is 0.4.

Fig. 19 Illustration of the Fiducial Volume Trigger. The interaction is assumed to take place in the exit window of the bubble chamber. An identical extrapolation is done for the entrance window. Full lines correspond to real tracks and broken lines to the FVT computations.

Fig. 20 Multiplicity distributions in 400 and 405 GeV/c pp interactions (histogram and points respectively). The distributions are normalized for $N_{ch} > 8$, where the ratio between the number of entries in the bins of the two distributions is constant. The curve is a guide for the eye.

Fig. 21 HPD digitizations of the charm event shown in fig. 3. Note the different scales for the two directions.

Fig. 22 Momentum of reconstructed tracks: (a) all tracks, (b) tracks from charm decays and (c) all tracks entering the second lever arm.

Fig. 23 φ angle (bending plane) of measured and reconstructed (hatched) tracks in LEBC. The losses for small φ values are mainly due to the λ angle (non−bending plane) being out of acceptance (compare fig. 24).

Fig. 24 λ angle acceptance, given by the ratio of The number of reconstructed to measured tracks. A cut in φ at 75 mrad removes most influence of φ angle acceptance.

Fig. 25 φ angle of reconstructed tracks in the second lever arm, with a hit in the drift chamber D4.

Fig. 26 Monte Carlo estimated acceptance in Cherenkov detector SAD and into the second lever arm, as a function of the momentum resolution. The M1 currents are: A) 670, B) 880, C) 1080, D) 1280 and E) 1480 A.

Fig. 27 Spectrometer acceptance for neutral D−mesons obtaining three constrained fits. The full line is for decays without neutral particles, the broken line with observed neutrals.

Fig. 28 Momentum resolution. The three histograms show (a) all tracks, (b) tracks in the first lever arm and (c) tracks in the second lever arm.

Fig. 29 Invariant mass of all combinations of measured tracks from two−body decays: (a) $\pi^+\pi^-$, (b) $p\pi^-$ and (c) $\bar{p}\pi^+$ combinations in the K^0 and $\Lambda^0/\overline{\Lambda^0}$ regions.

Fig. 30 Mass of D^0 obtained from two and four−prong charm decays with all tracks reconstructed. All Cabibbo favoured combinations which are compatible with the particle identification are included.

Fig. 31 Unique identification in ISIS as a function of momentum. In this plot, the unique identification is defined by a mass hypothesis with a probability $< 1/10$ of the highest being rejected.

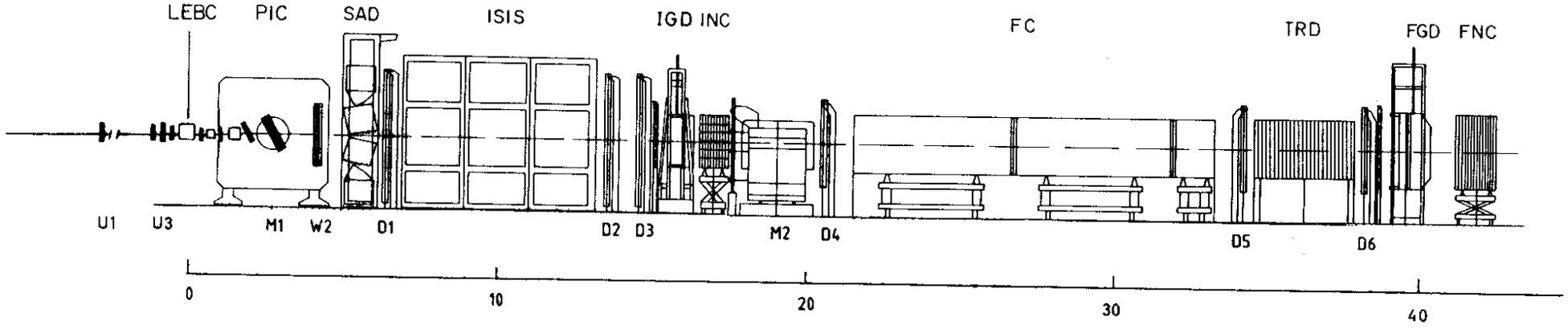
LEBC
PIC
SAD
ISIS
IGD INC
FC
TRD
FGD
FNC
U1
U3
M1
W2
D1
D2
D3
M2
D4
D5
D6
0
10
20
30
40

Fig. 1

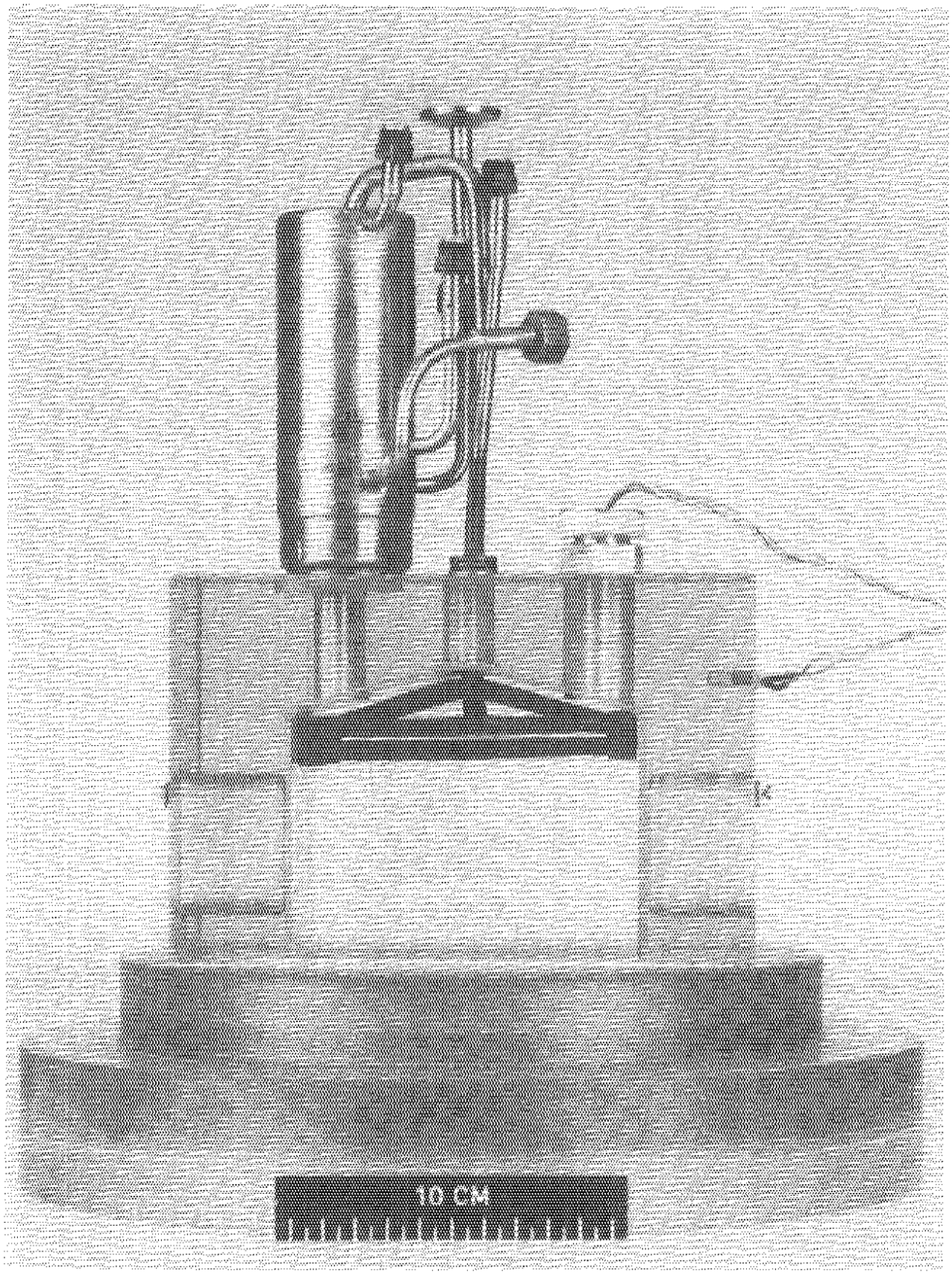

Fig. 2 (a)

Fig. 2 (b)

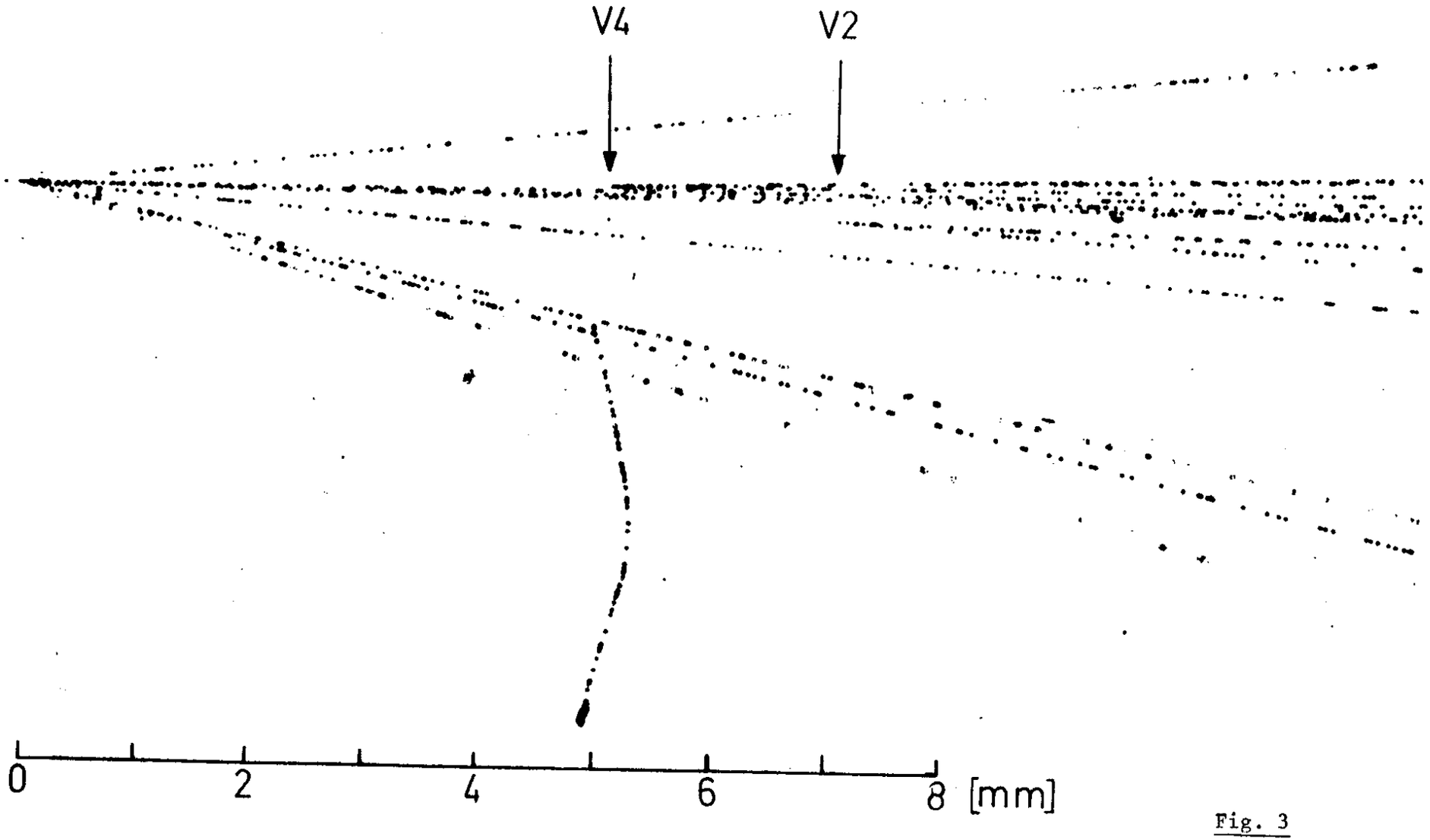

Fig. 3

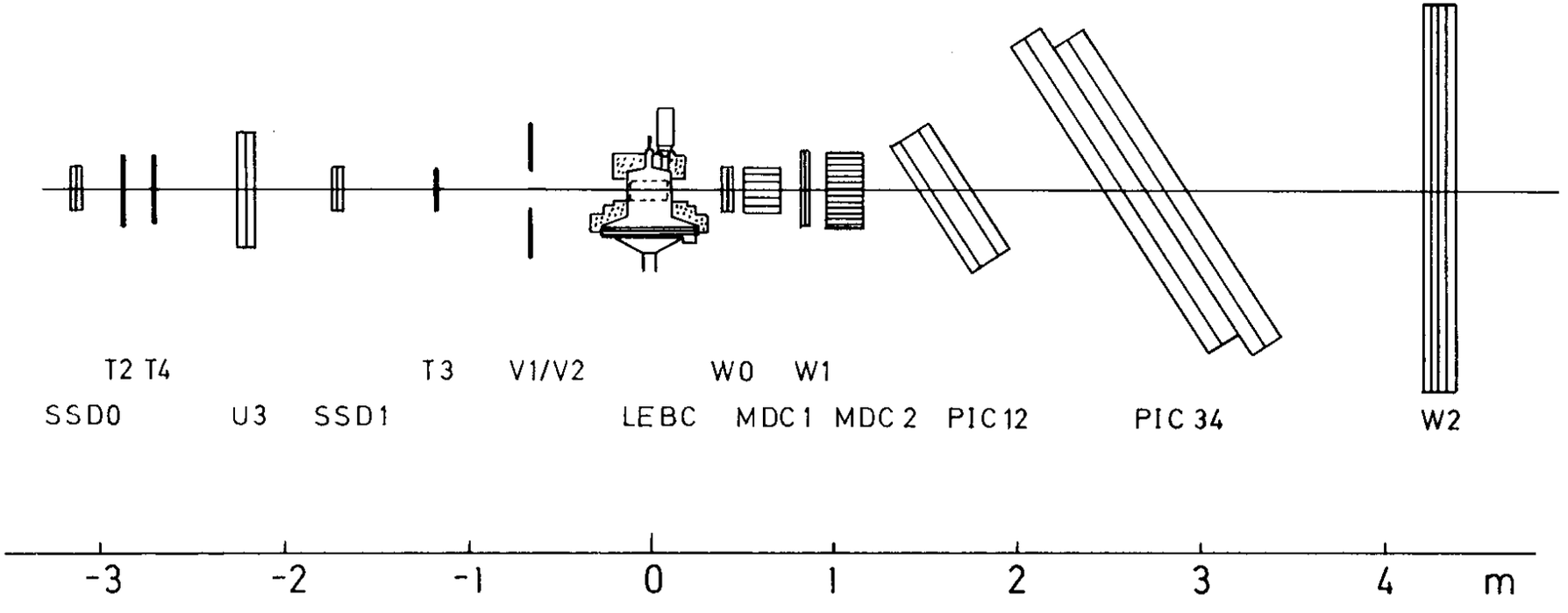
T2 T4
T3
V1/V2
W0
W1
SSD0
U3
SSD1
LEBC
MDC1
MDC2
PIC12
PIC34
W2
-3
-2
-1
0
1
2
3
4
m

Fig. 4

Fig. 5

Fig. 6

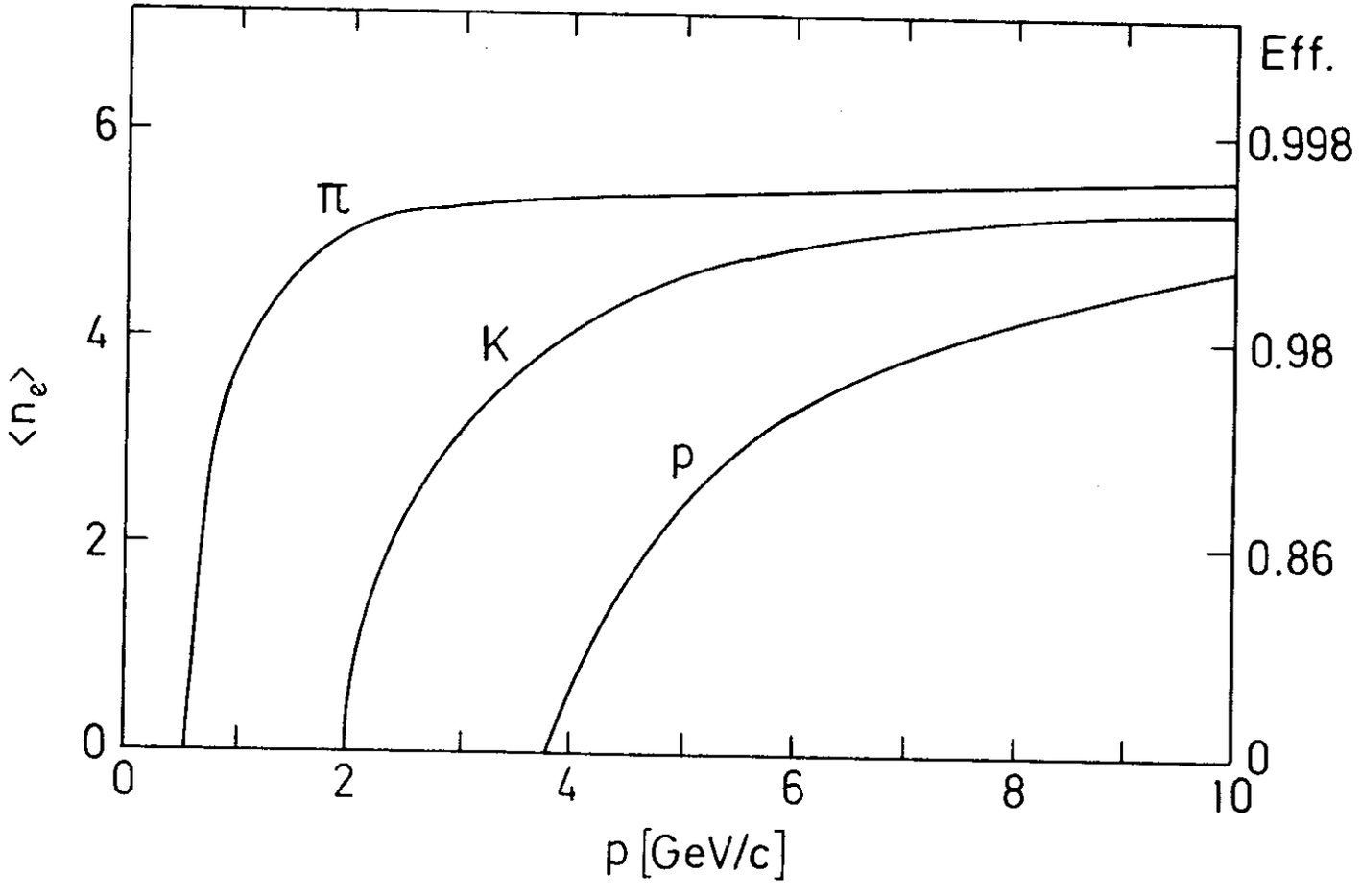

Fig. 7

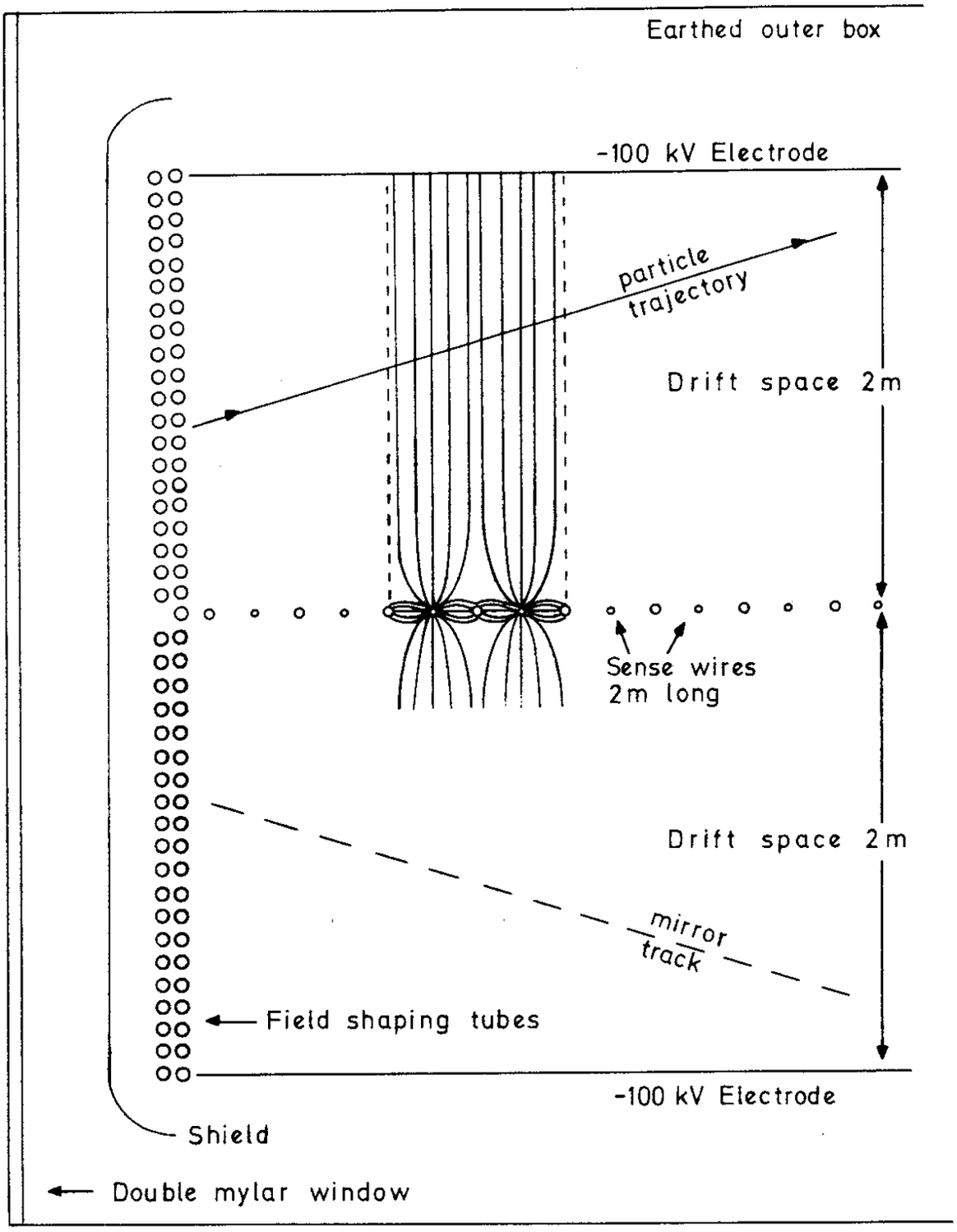
Earthed outer box
-100 kV Electrode
particle trajectory
Drift space 2m
Sense wires 2m long
Drift space 2m
mirror track
Field shaping tubes
-100 kV Electrode
Shield
Double mylar window

Fig. 8

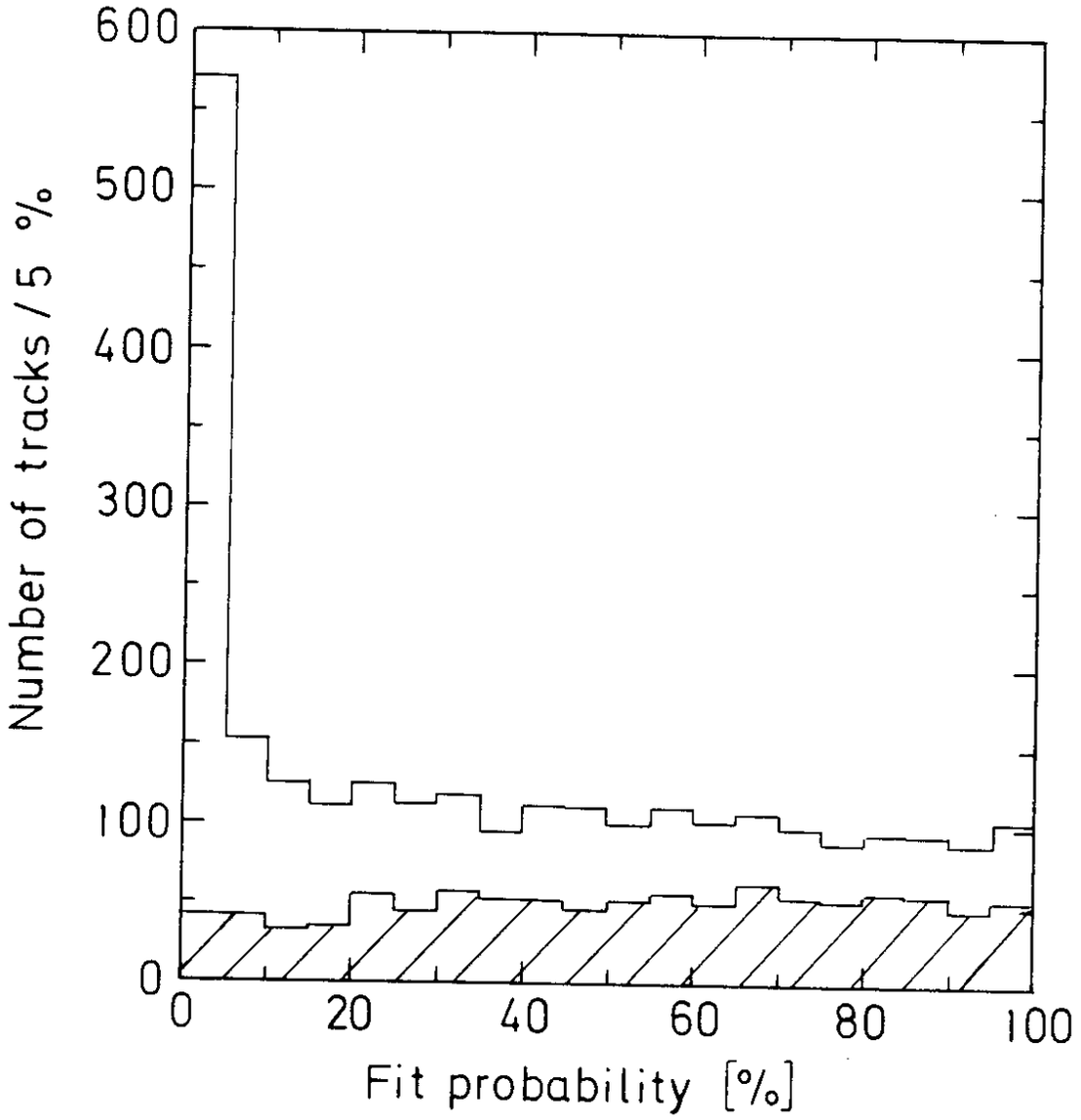
600
500
400
300
200
100
0
Number of tracks / 5 %
0
20
40
60
80
100
Fit probability [%]

Fig. 9

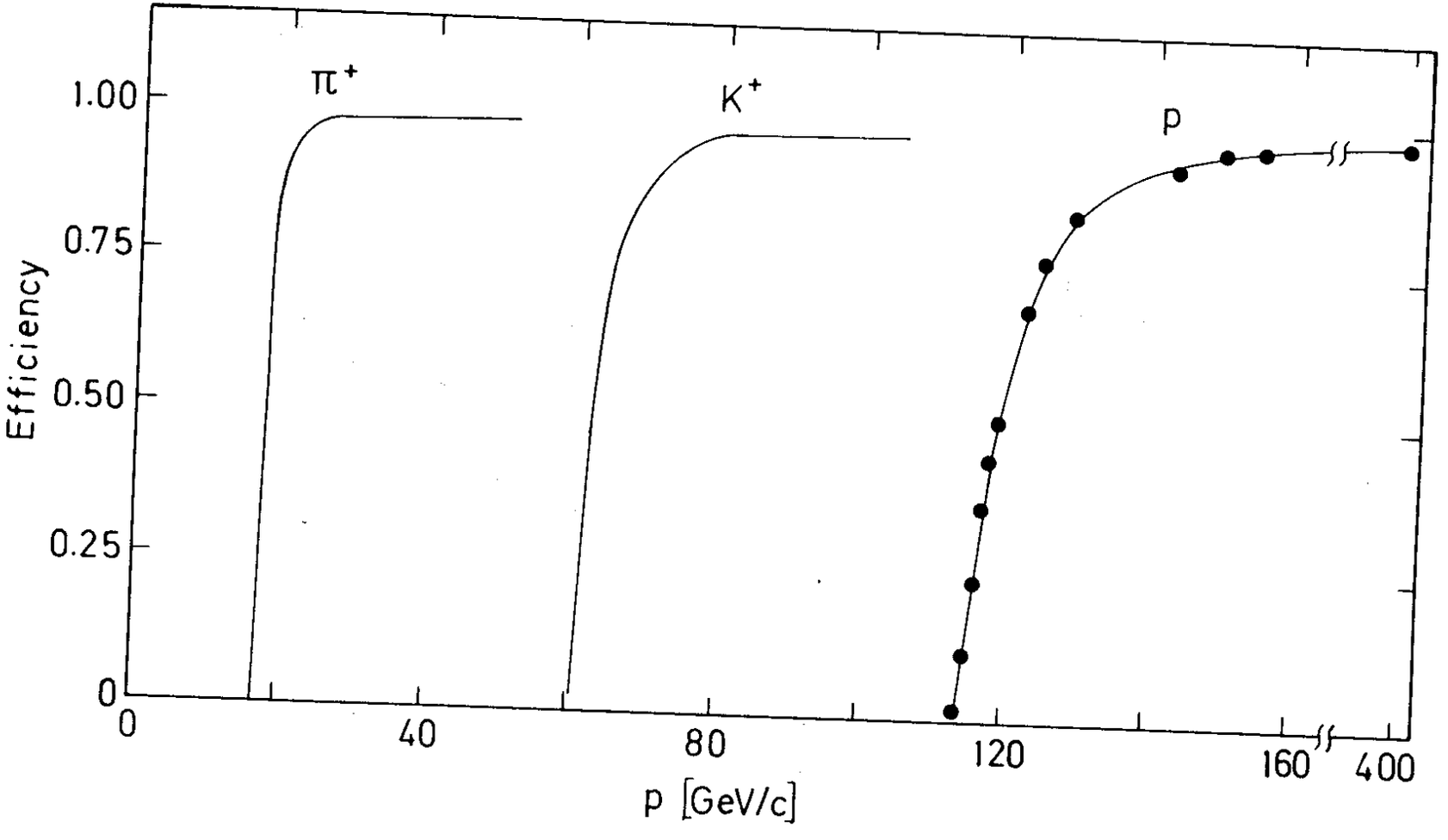

Fig. 10

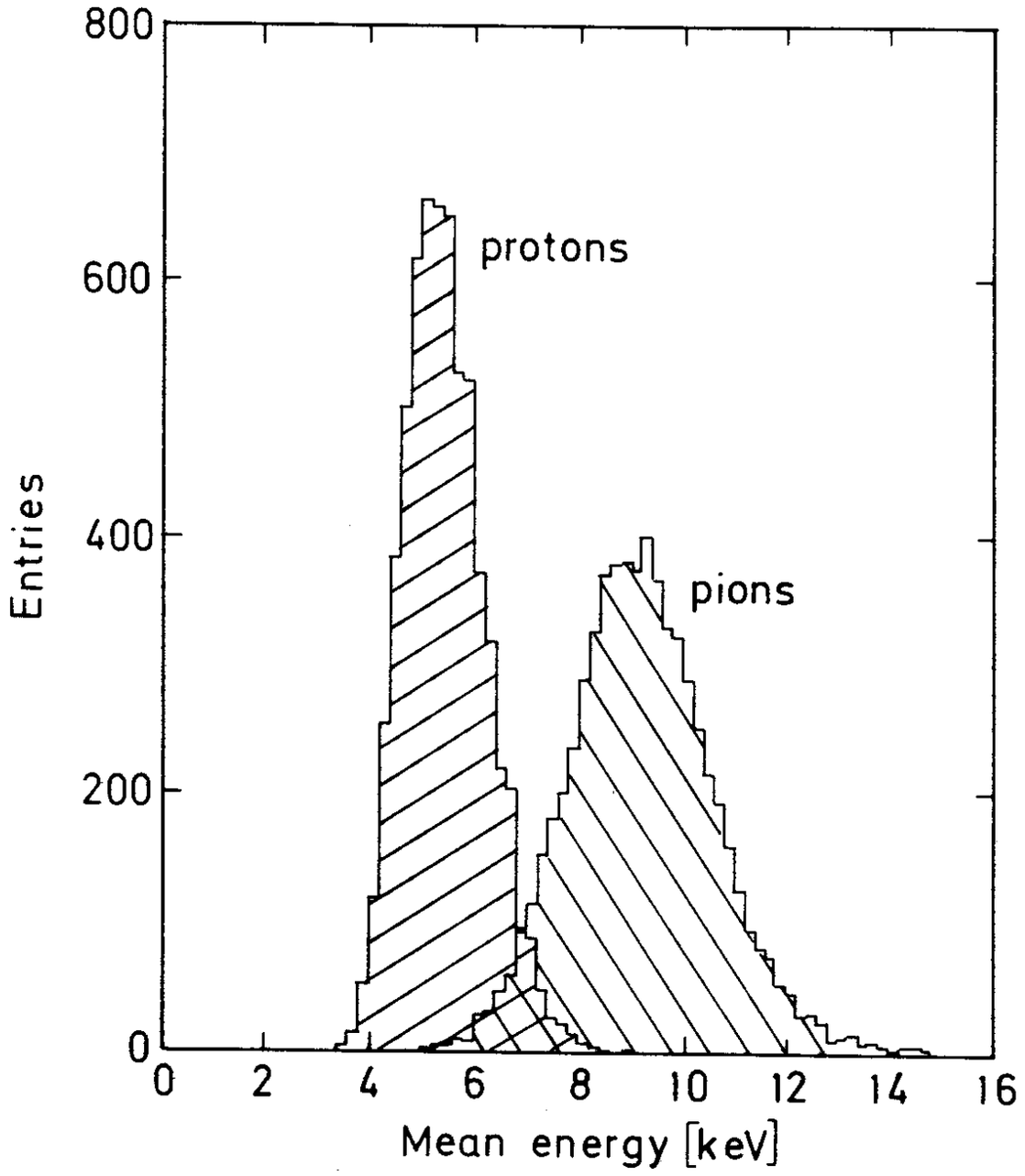
800
600
400
200
0
Entries
protons
pions
0
2
4
6
8
10
12
14
16
Mean energy [keV]

Fig. 11

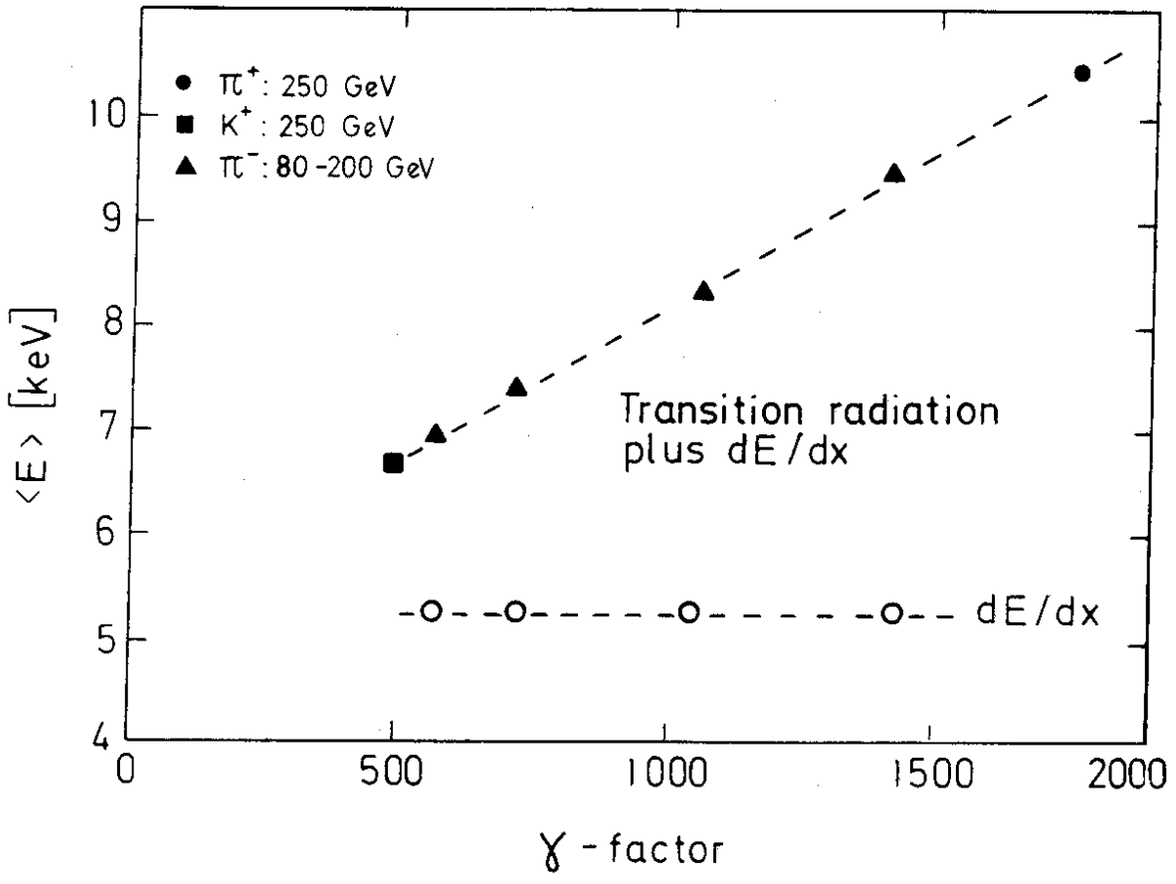
● π⁺: 250 GeV
■ K⁺: 250 GeV
▲ π⁻: 80-200 GeV
Transition radiation
plus dE/dx
dE/dx
<E> [keV]
γ - factor
0
500
1000
1500
2000
4
5
6
7
8
9
10

Fig. 12

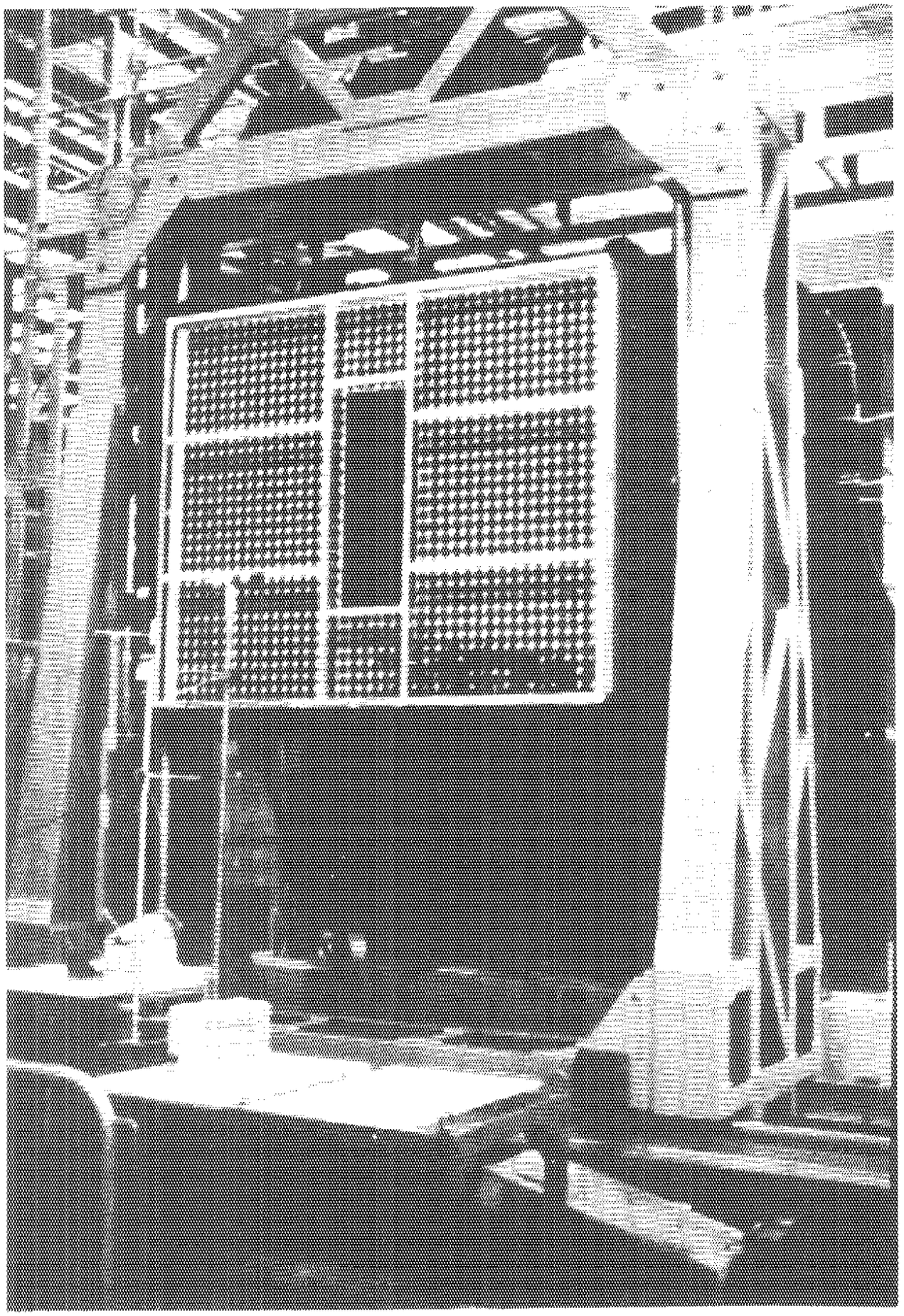

Fig. 13

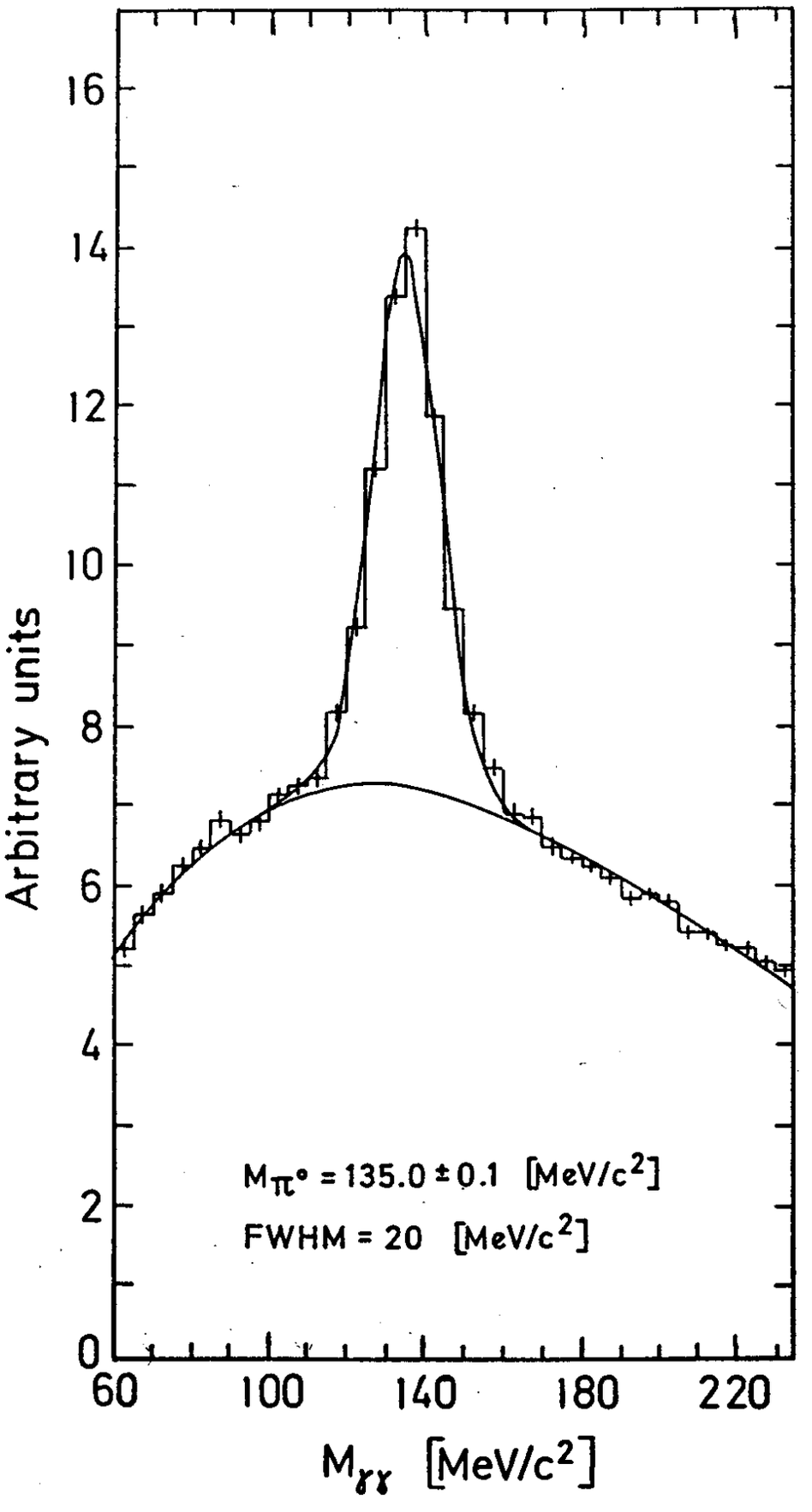
16
14
12
10
8
6
4
2
0
Arbitrary units
M_{π^0} = 135.0 ± 0.1 [MeV/c^2]
FWHM = 20 [MeV/c^2]
60
100
140
180
220
$M_{\gamma\gamma}$ [MeV/c^2]

Fig. 14

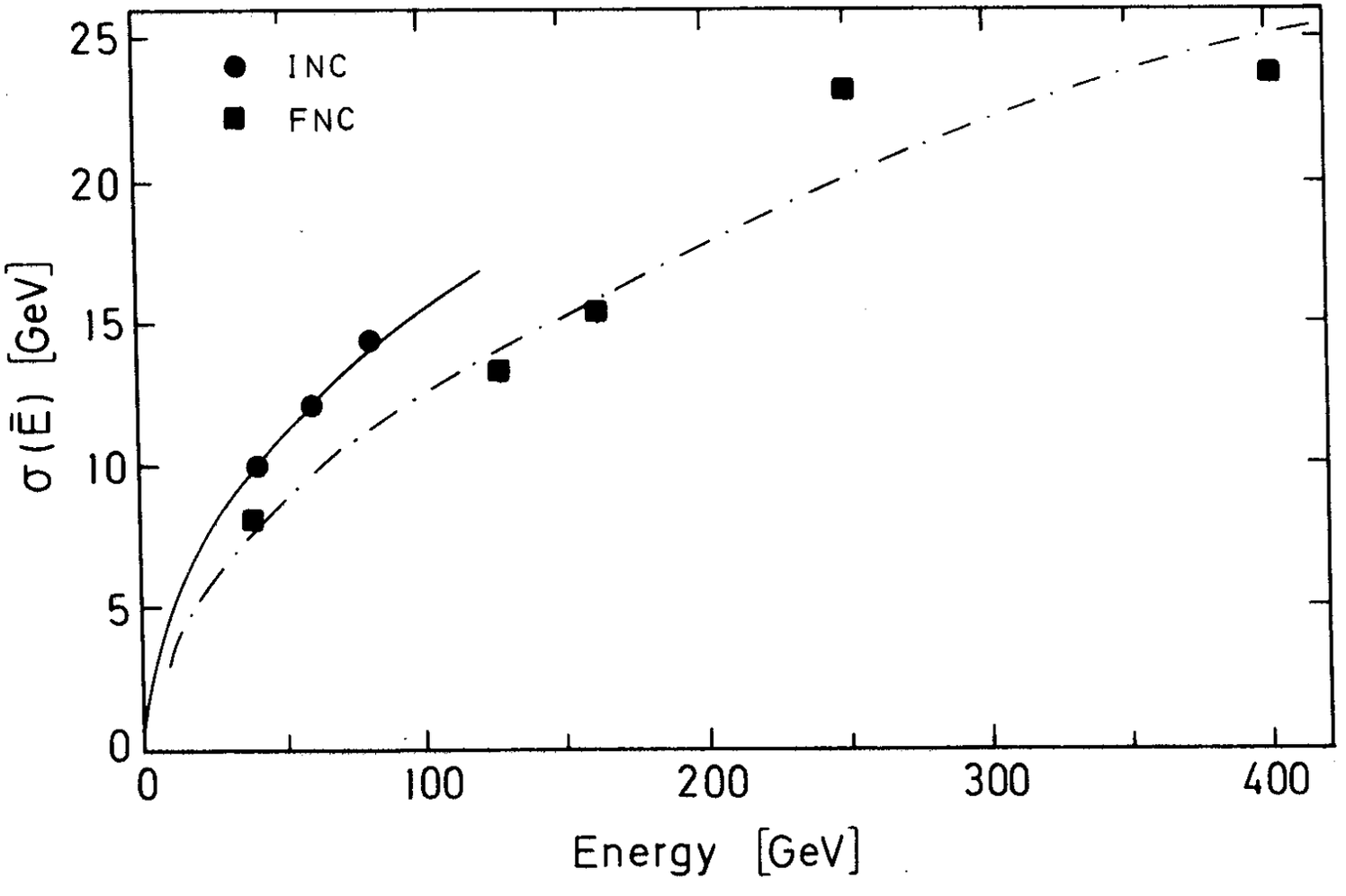

Fig. 16

FNC cell

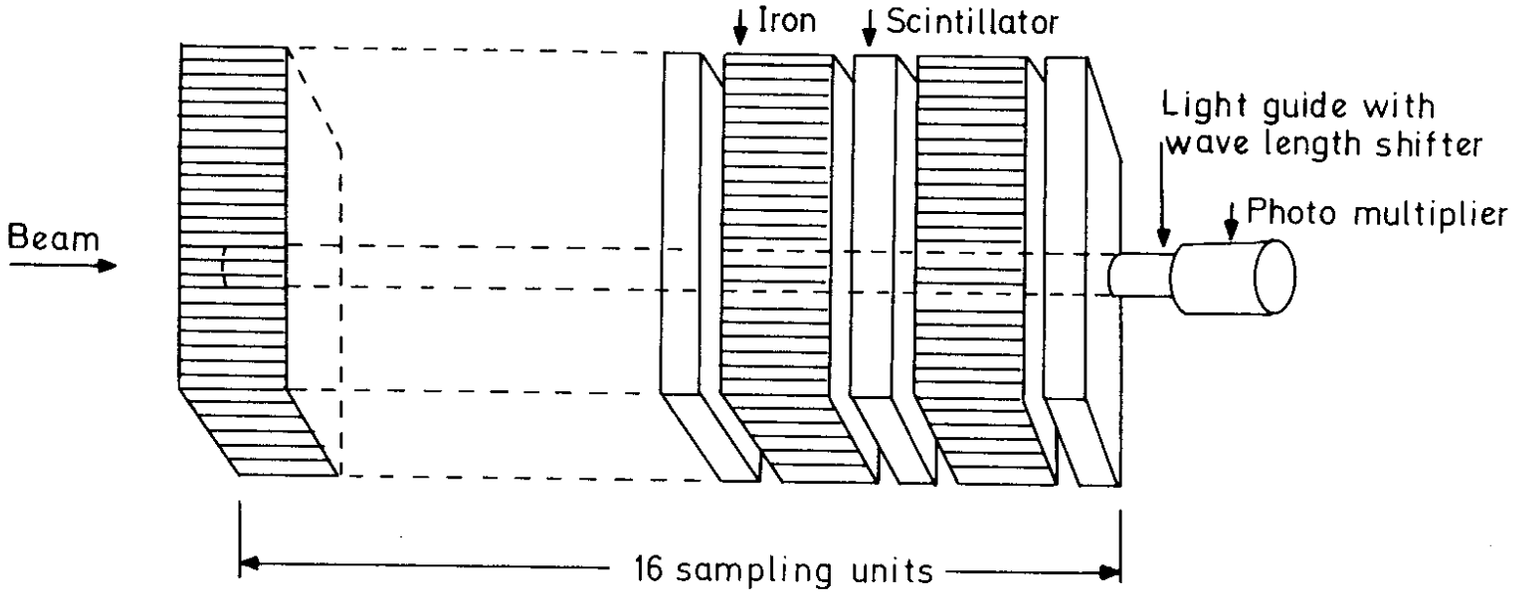

Fig. 17

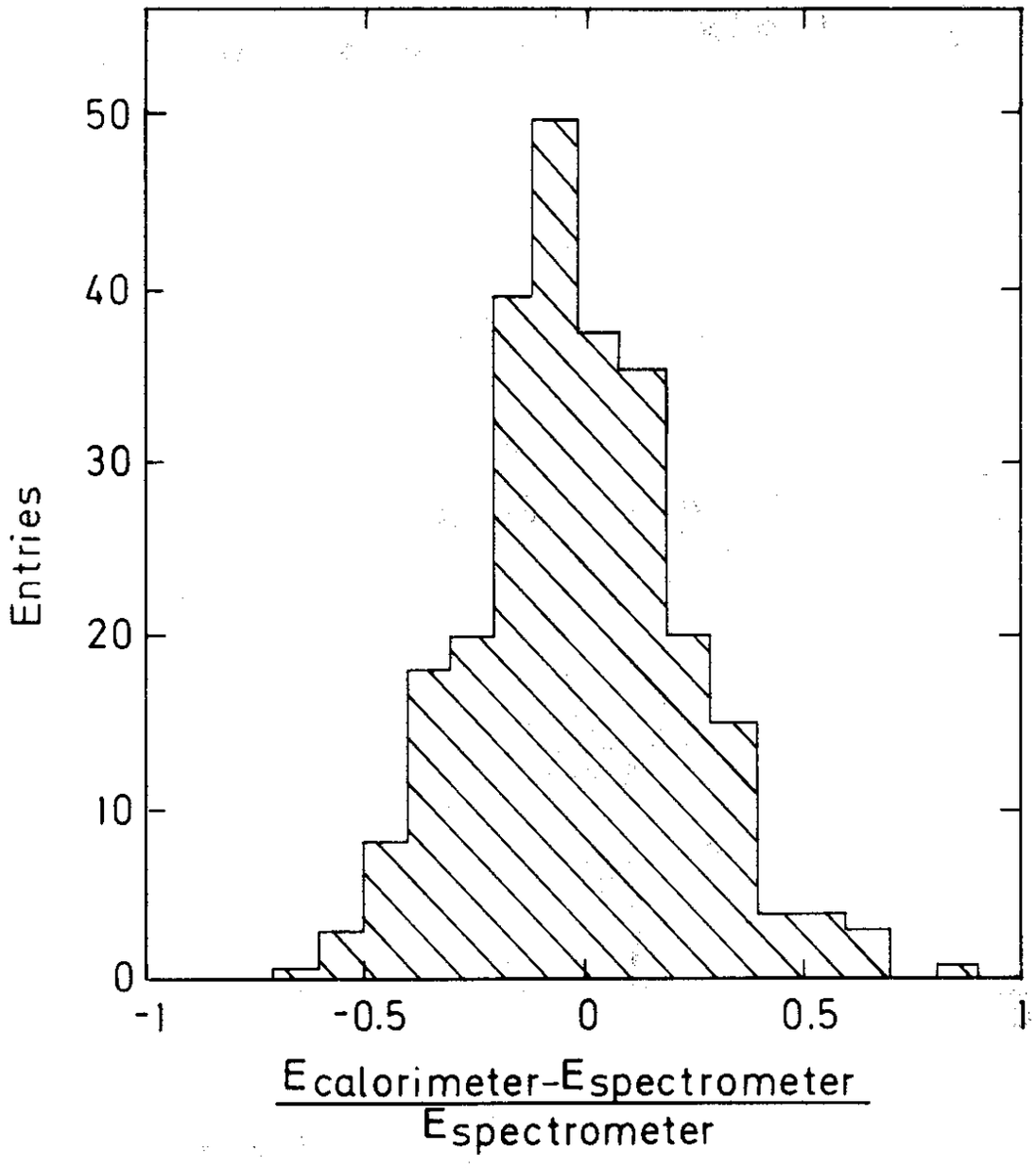
50
40
30
20
10
0
Entries
-1
-0.5
0
0.5
1
Ecalorimeter-Espectrometer
Espectrometer

Fig. 18

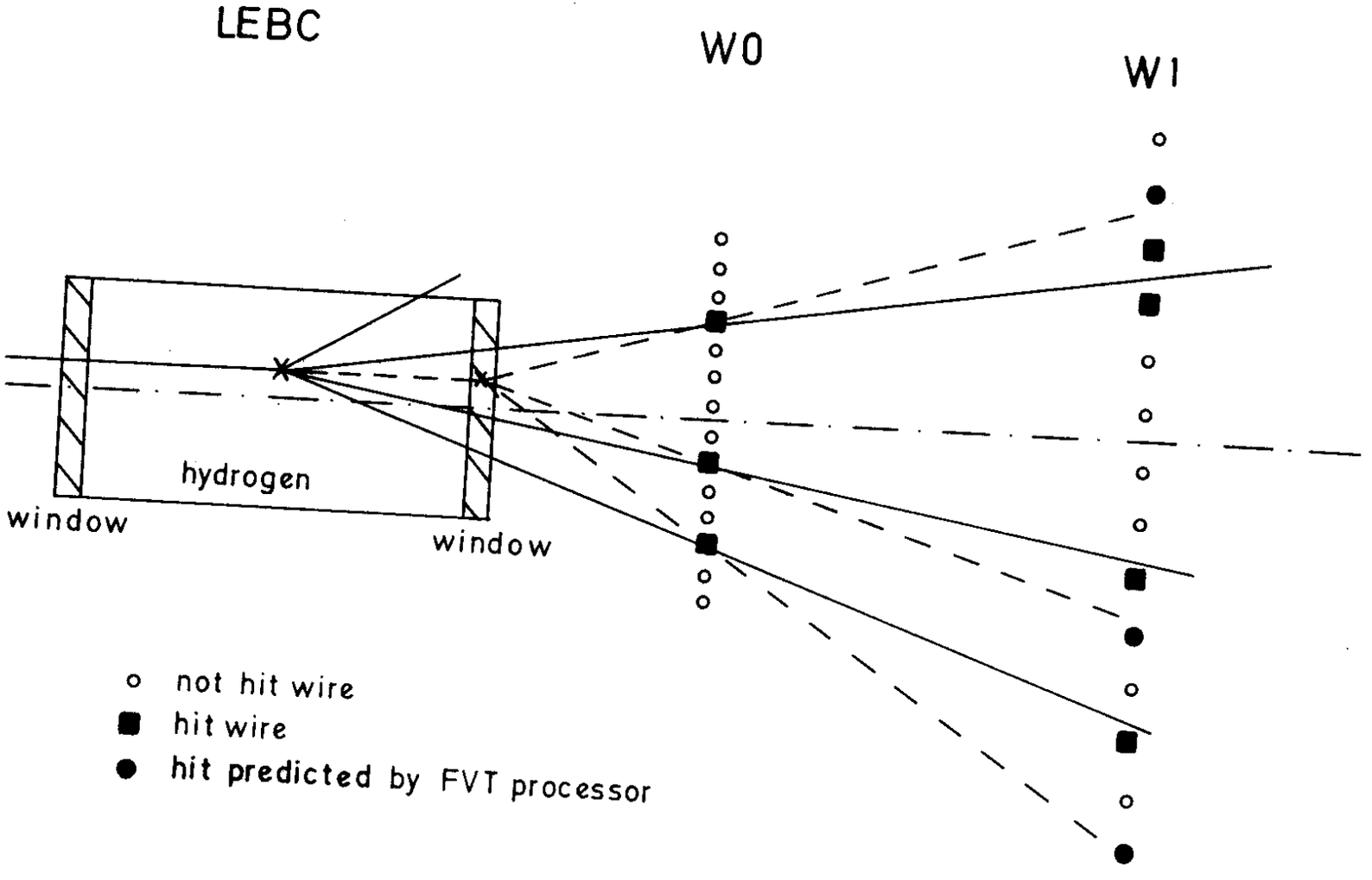
LEBC
W0
W1
hydrogen
window
window
not hit wire
hit wire
hit predicted by FVT processor

Fig. 19

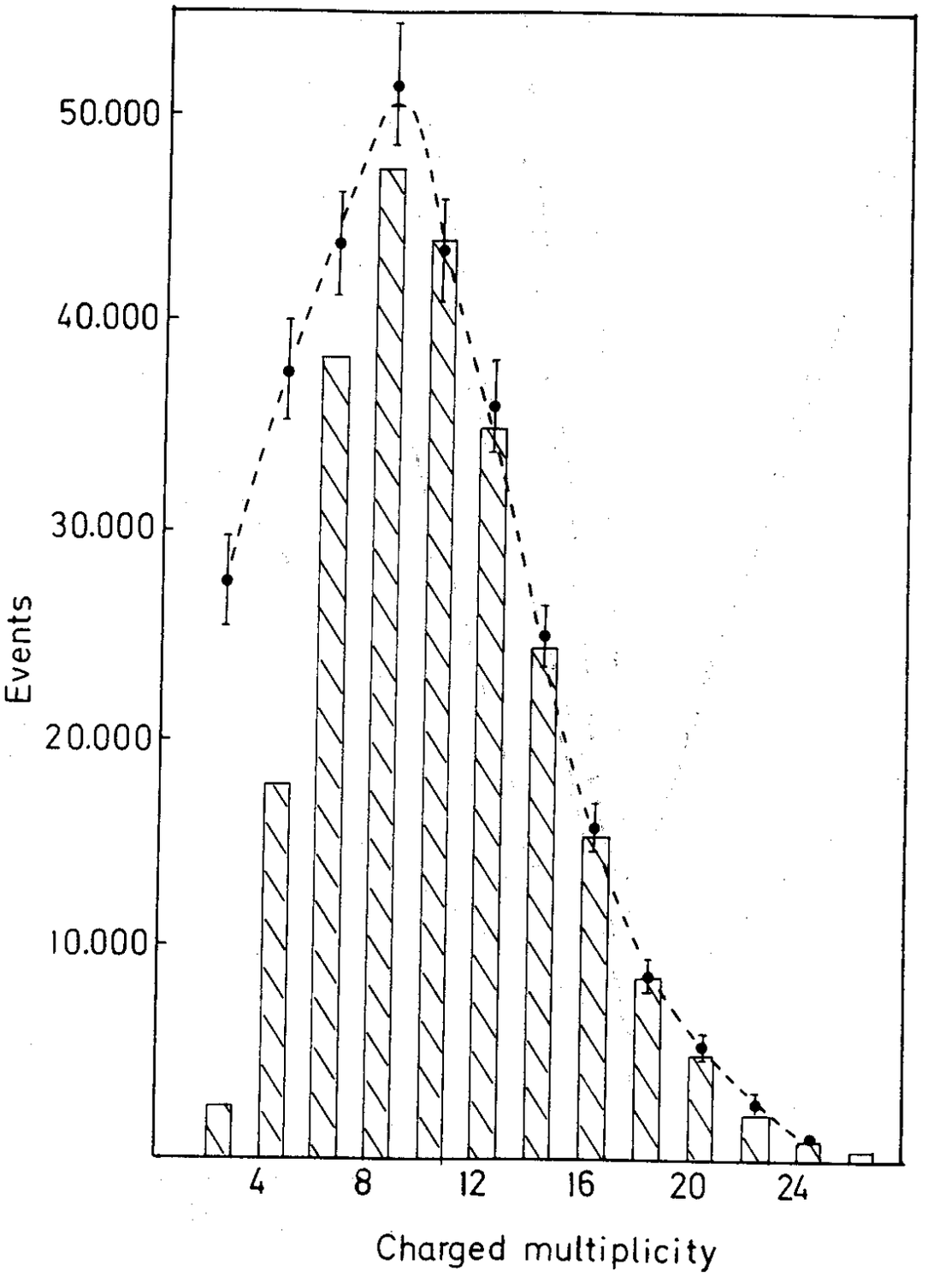
50.000
40.000
30.000
20.000
10.000
Events
4
8
12
16
20
24
Charged multiplicity

Fig. 20

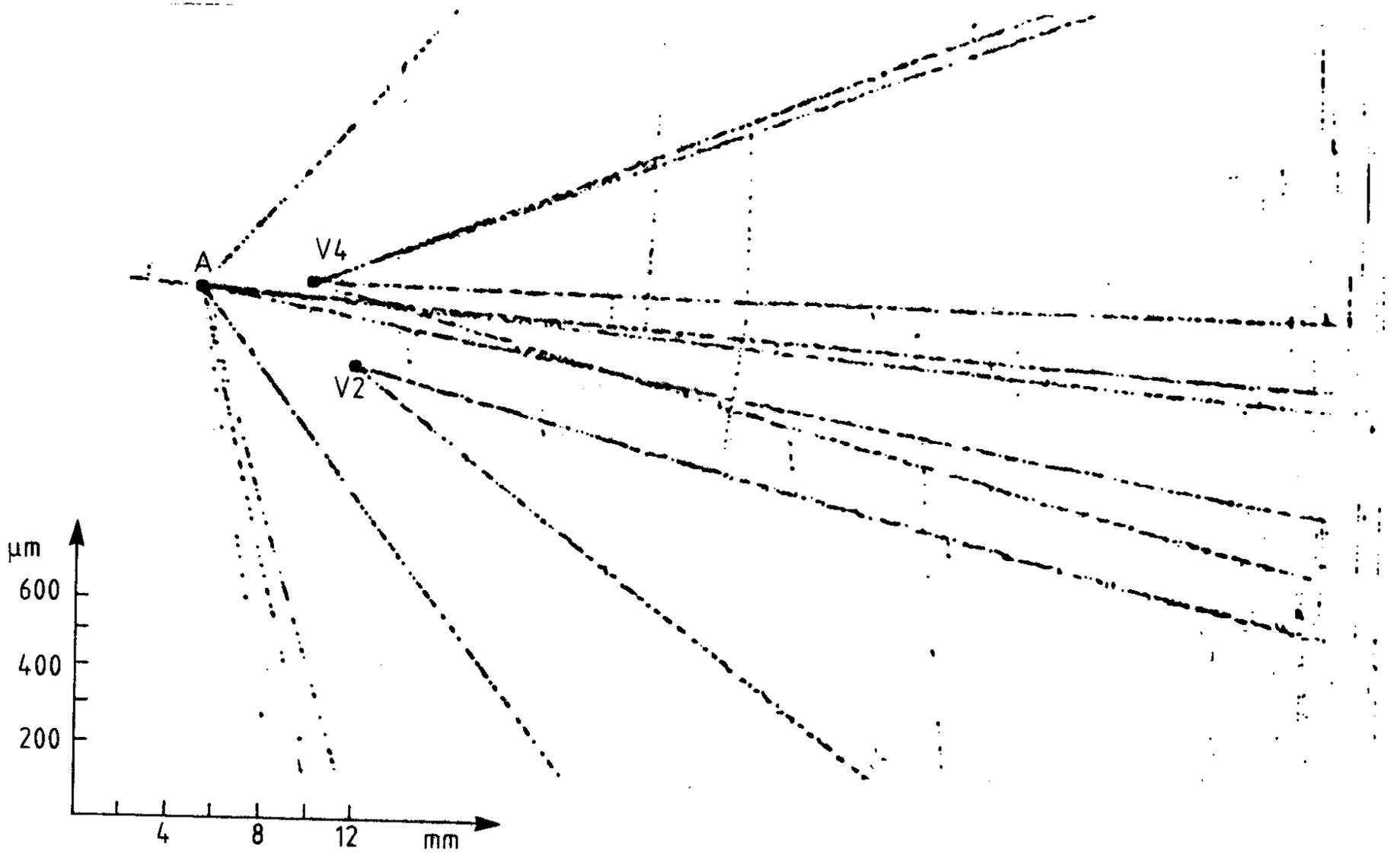

Fig. 21

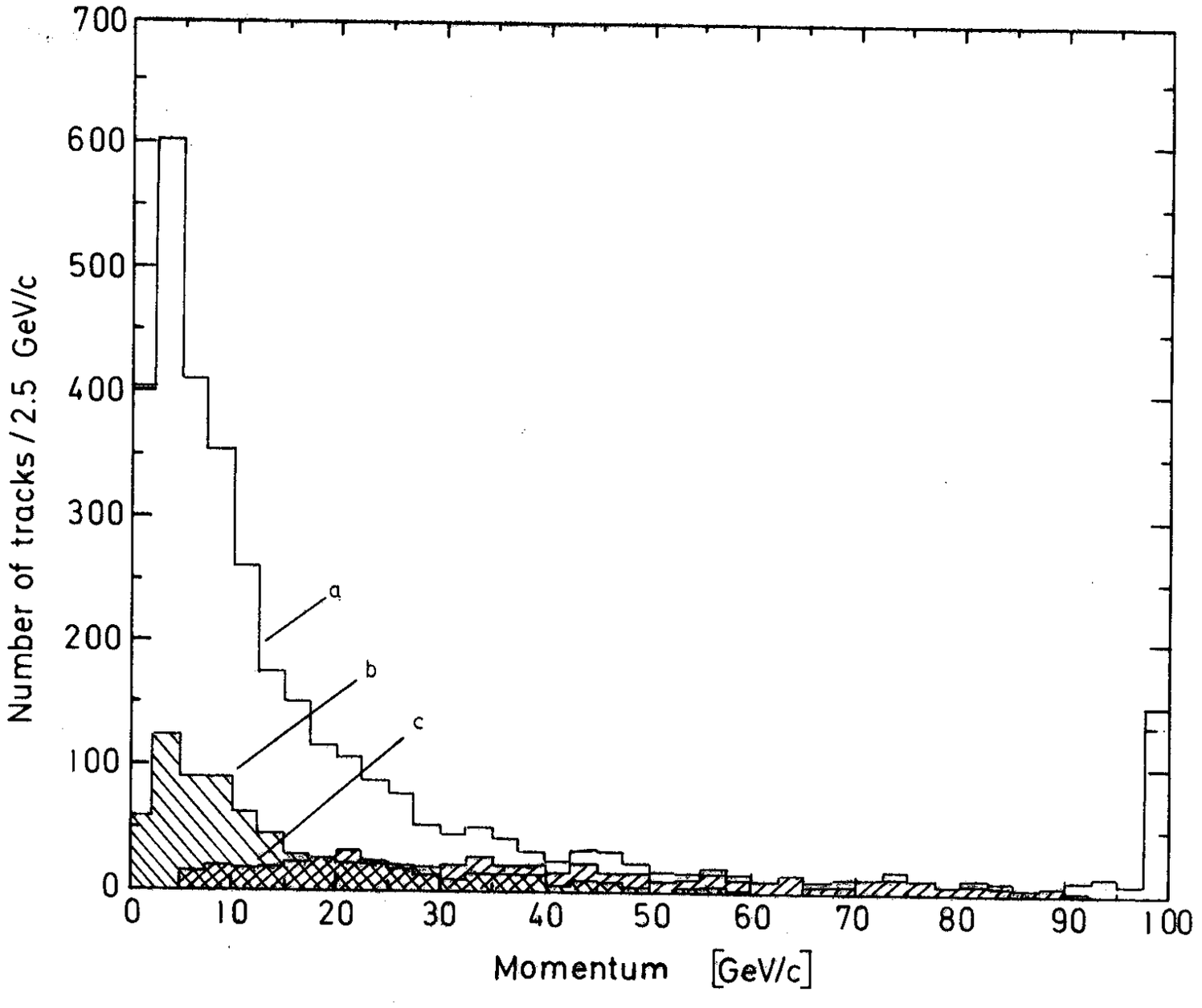
700
600
500
400
300
200
100
0
Number of tracks / 2.5 GeV/c
a
b
c
0
10
20
30
40
50
60
70
80
90
100
Momentum [GeV/c]

Fig. 22

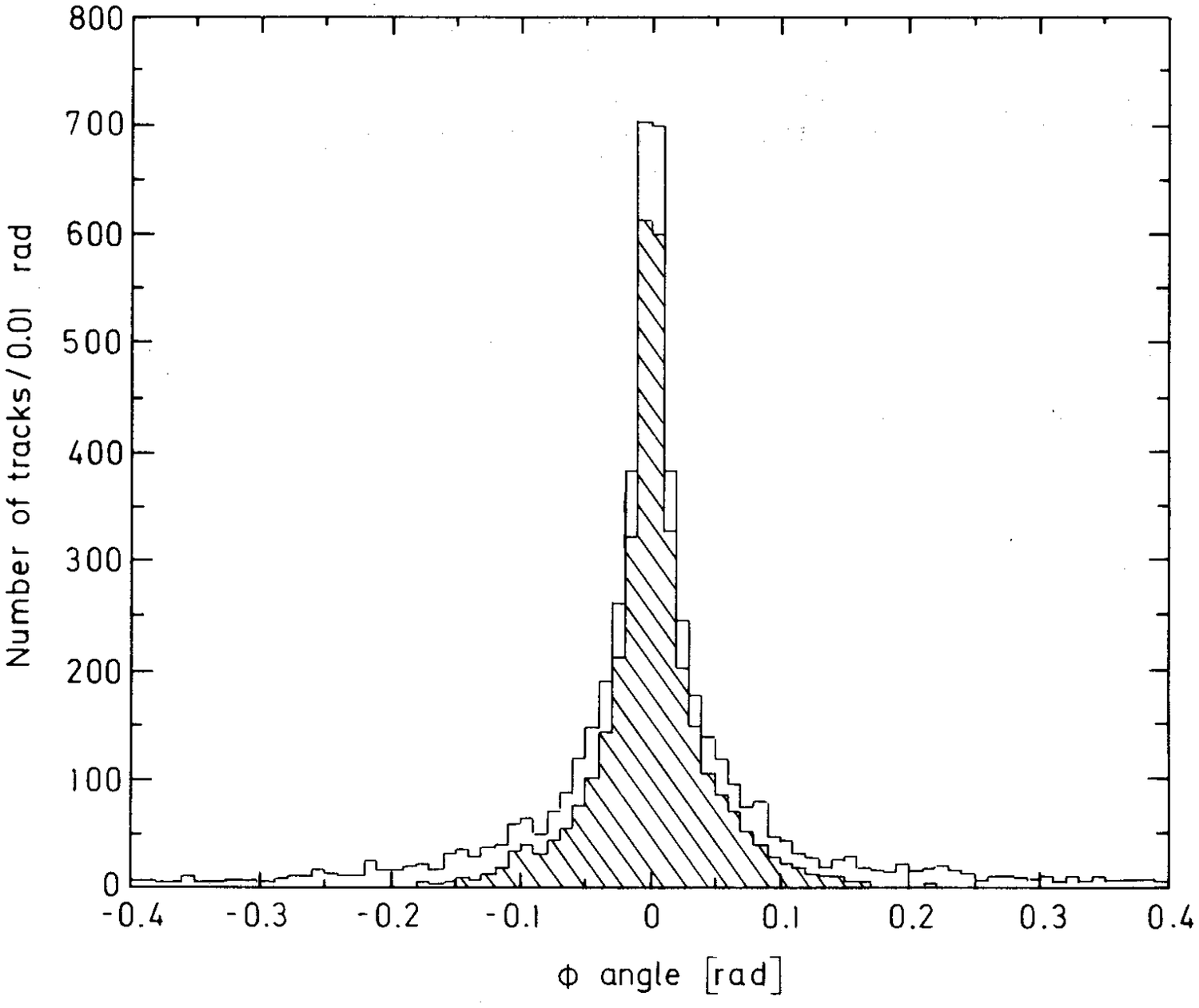
800
700
600
500
400
300
200
100
0
Number of tracks / 0.01 rad
-0.4
-0.3
-0.2
-0.1
0
0.1
0.2
0.3
0.4
Φ angle [rad]

Fig. 23

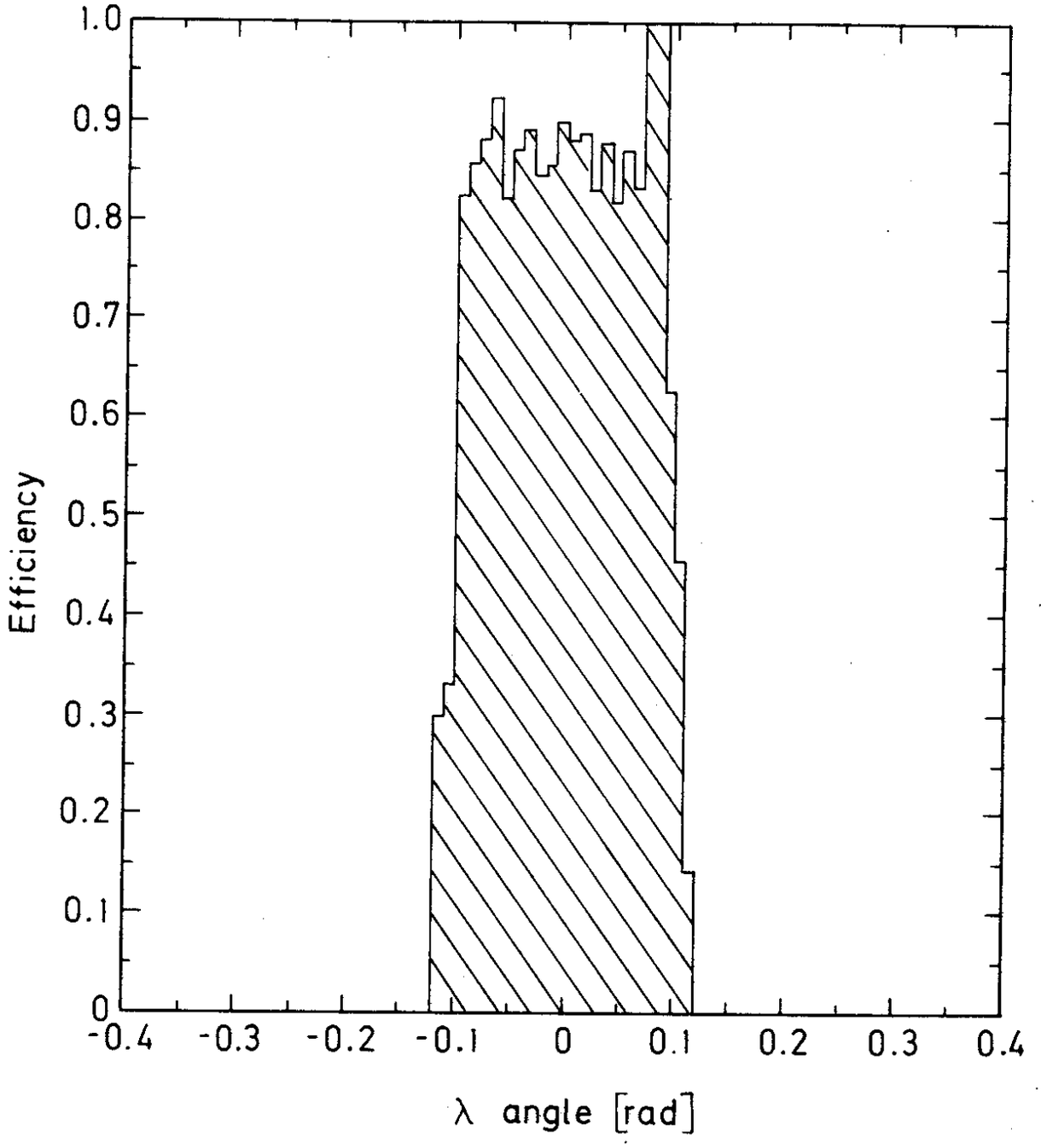
1.0
0.9
0.8
0.7
0.6
0.5
0.4
0.3
0.2
0.1
0
Efficiency
-0.4
-0.3
-0.2
-0.1
0
0.1
0.2
0.3
0.4
λ angle [rad]

Fig. 24

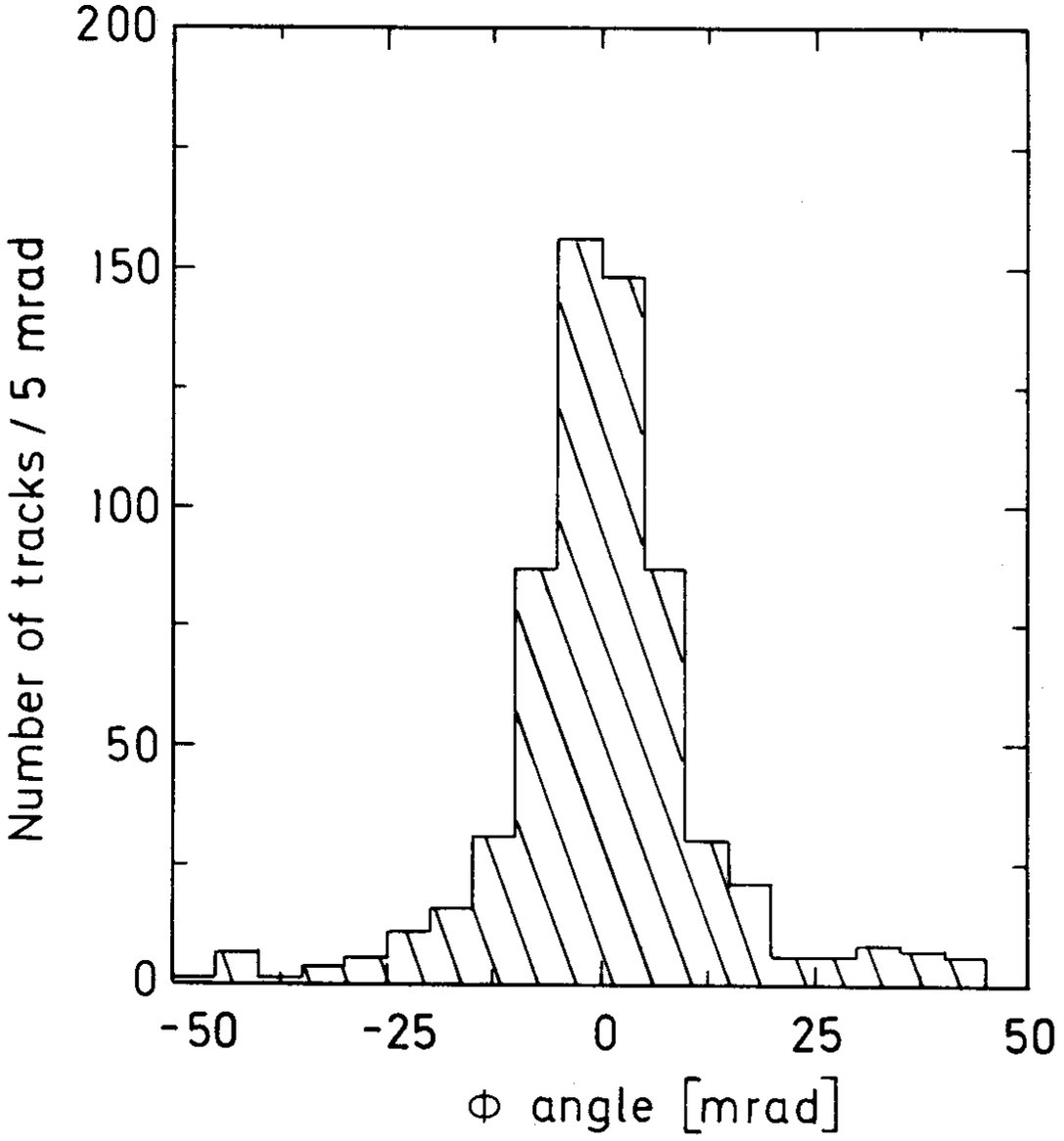
200
150
100
50
0
Number of tracks / 5 mrad
-50
-25
0
25
50
Φ angle [mrad]

Fig. 25

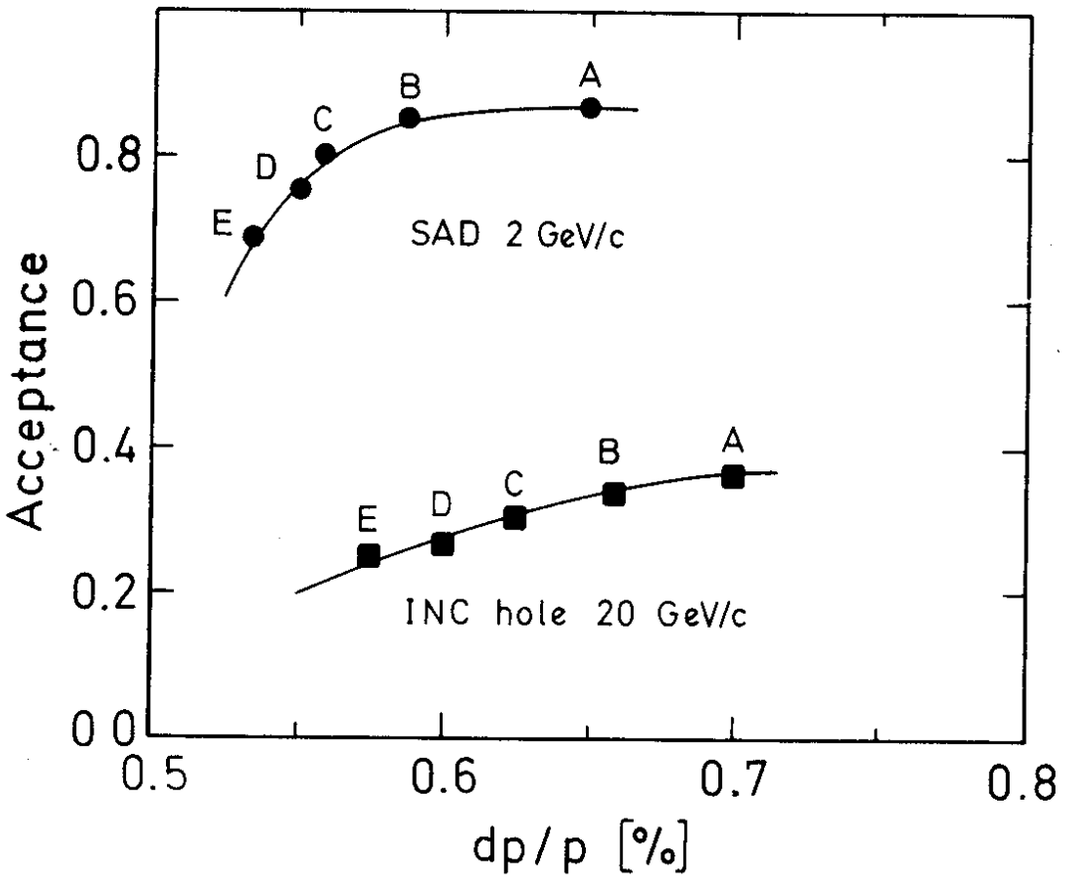
Acceptance
0.8
0.6
0.4
0.2
0 0
0.5
0.6
0.7
0.8
dp/p [%]
A
B
C
D
E
SAD 2 GeV/c
A
B
C
D
E
INC hole 20 GeV/c

Fig. 26

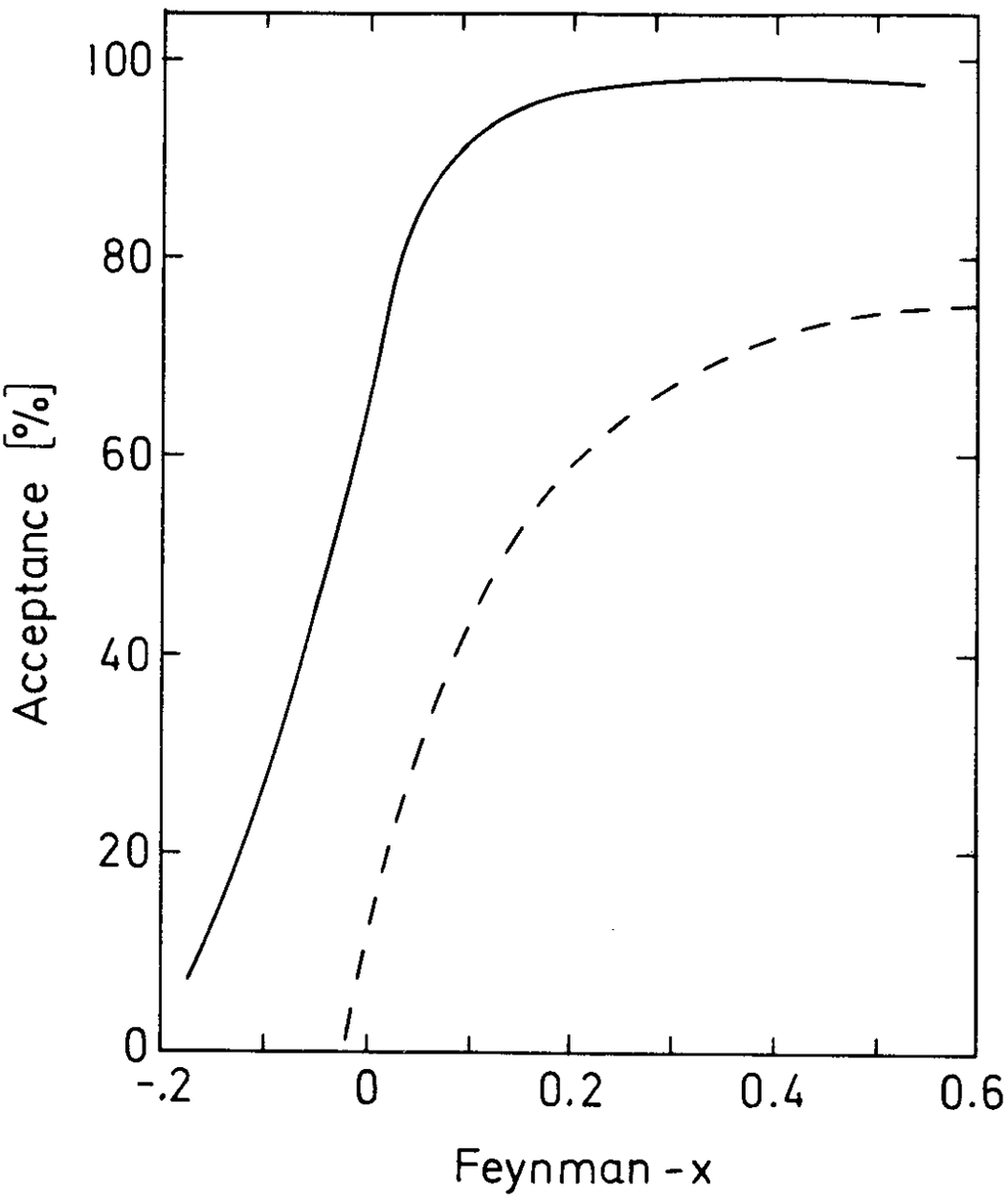

Fig. 27

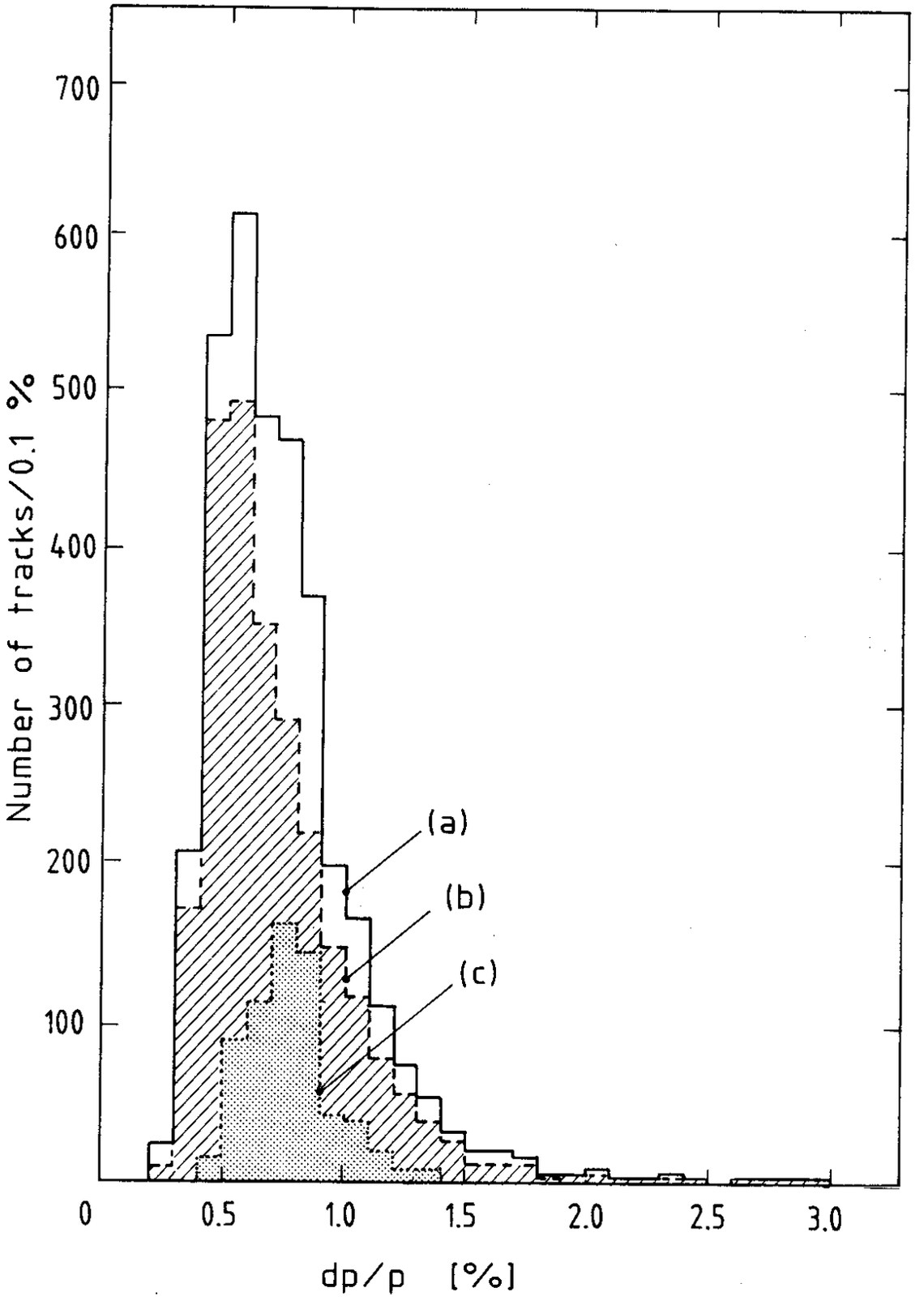
700
600
500
400
300
200
100
Number of tracks/0.1 %
(a)
(b)
(c)
0
0.5
1.0
1.5
2.0
2.5
3.0
dp/p [%]

Fig. 28

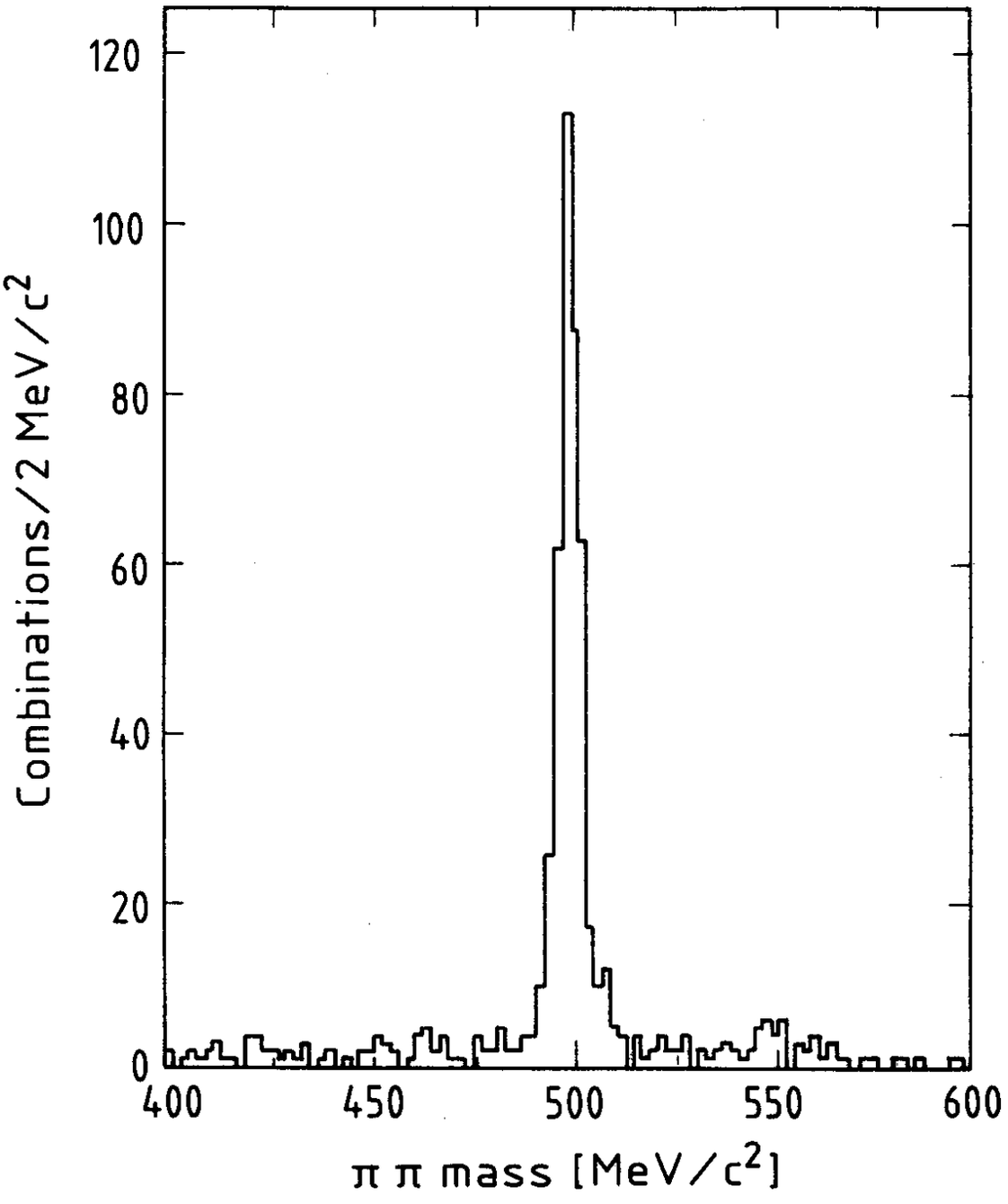
120
100
80
60
40
20
0
Combinations/2 MeV/c²
400
450
500
550
600
π π mass [MeV/c²]

Fig. 29 (a)

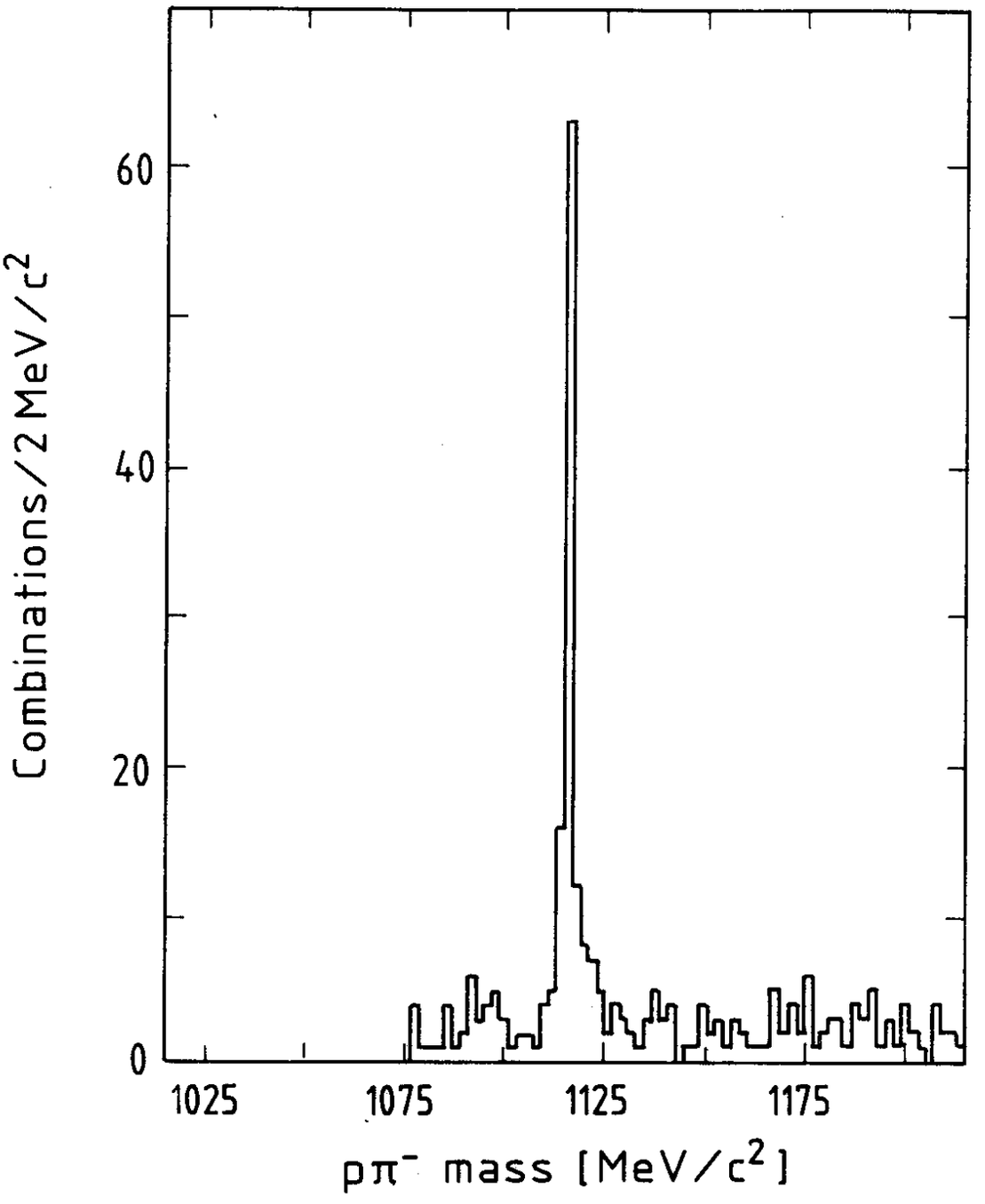
Combinations/2 MeV/c²
60
40
20
0
1025
1075
1125
1175
pπ⁻ mass [MeV/c²]

Fig. 29 (b)

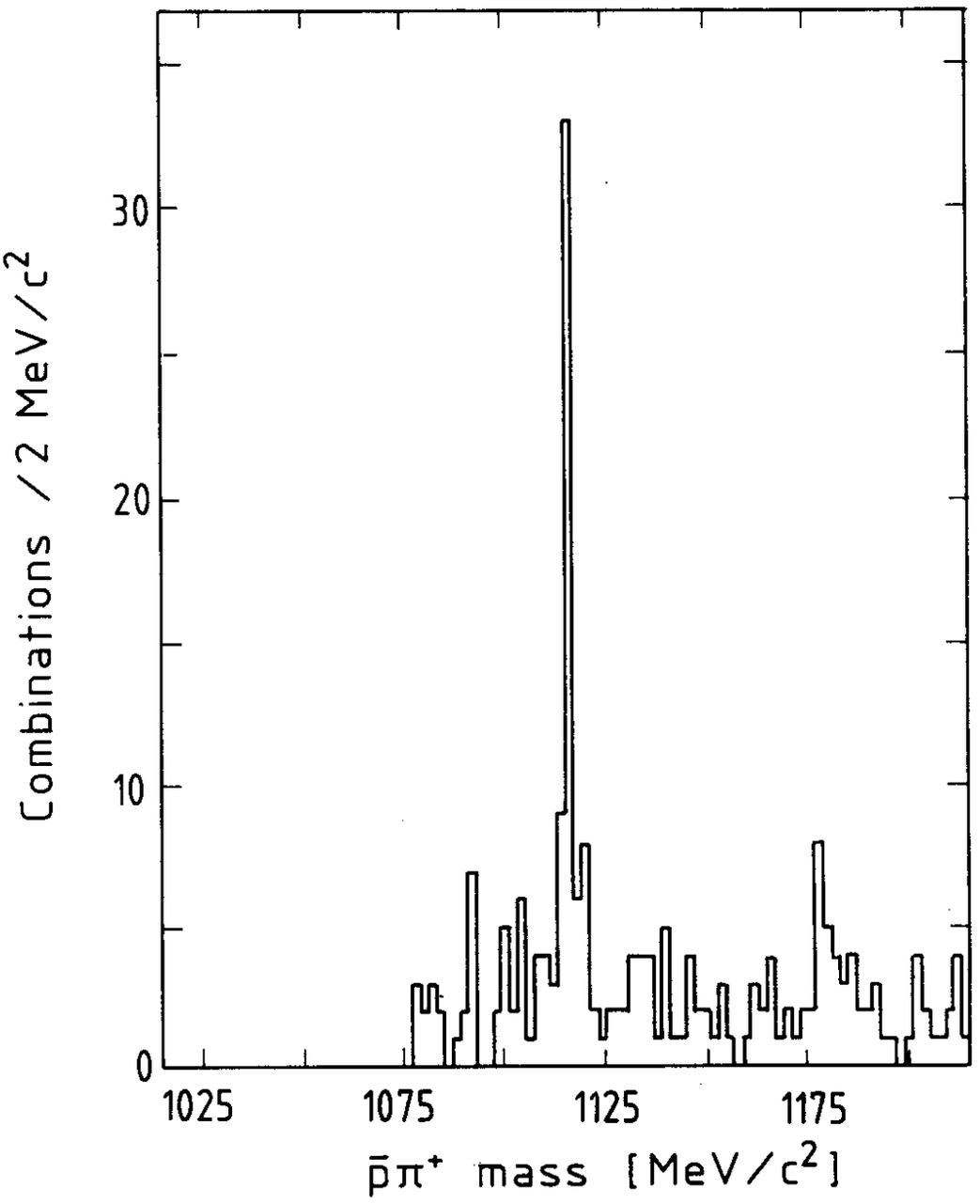
Combinations /2 MeV/c²
30
20
10
0
1025
1075
1125
1175
p̄π⁺ mass [MeV/c²]

Fig. 29 (c)

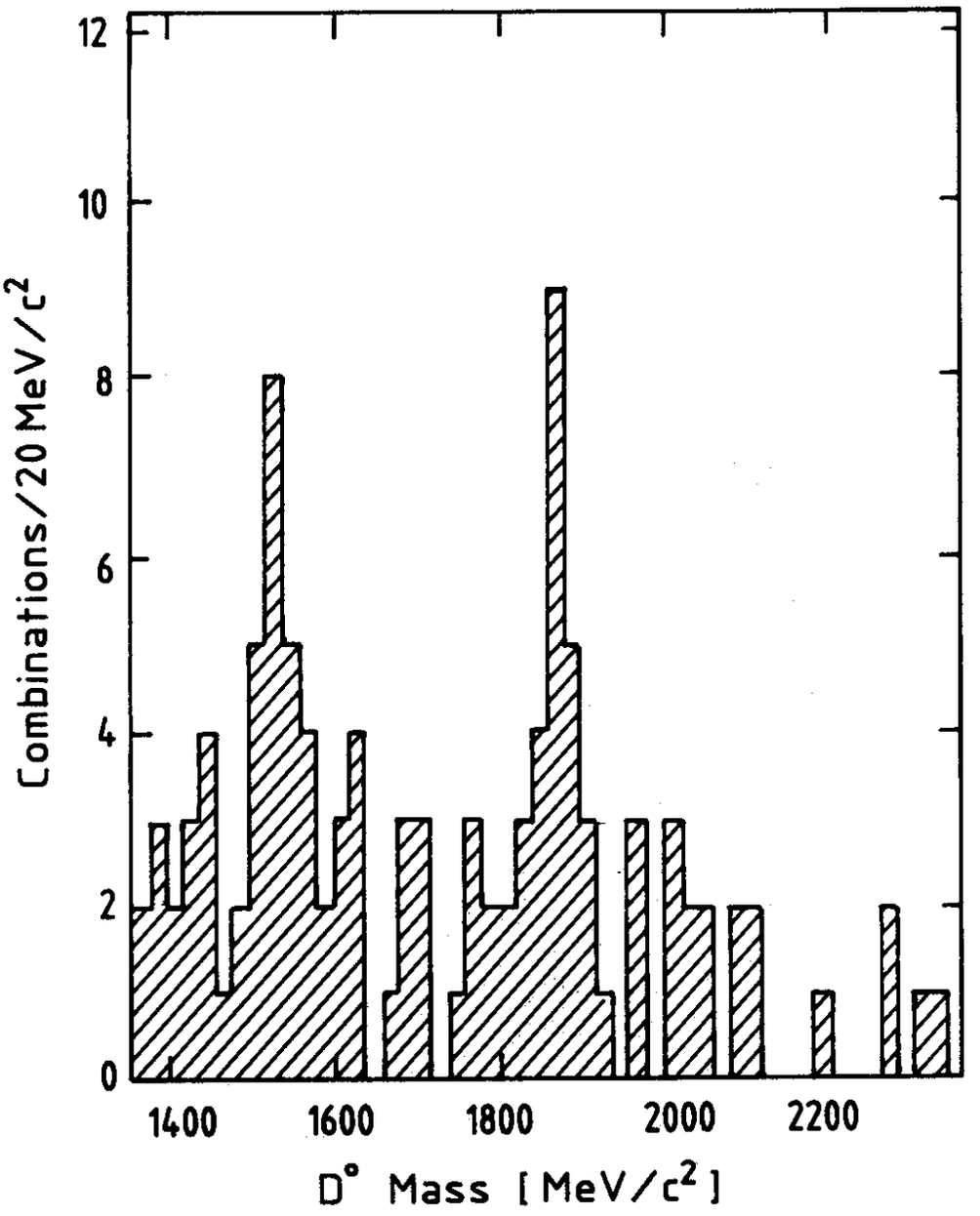
12
10
8
6
4
2
0
Combinations/20 MeV/c²
1400
1600
1800
2000
2200
D° Mass [MeV/c²]

Fig. 30

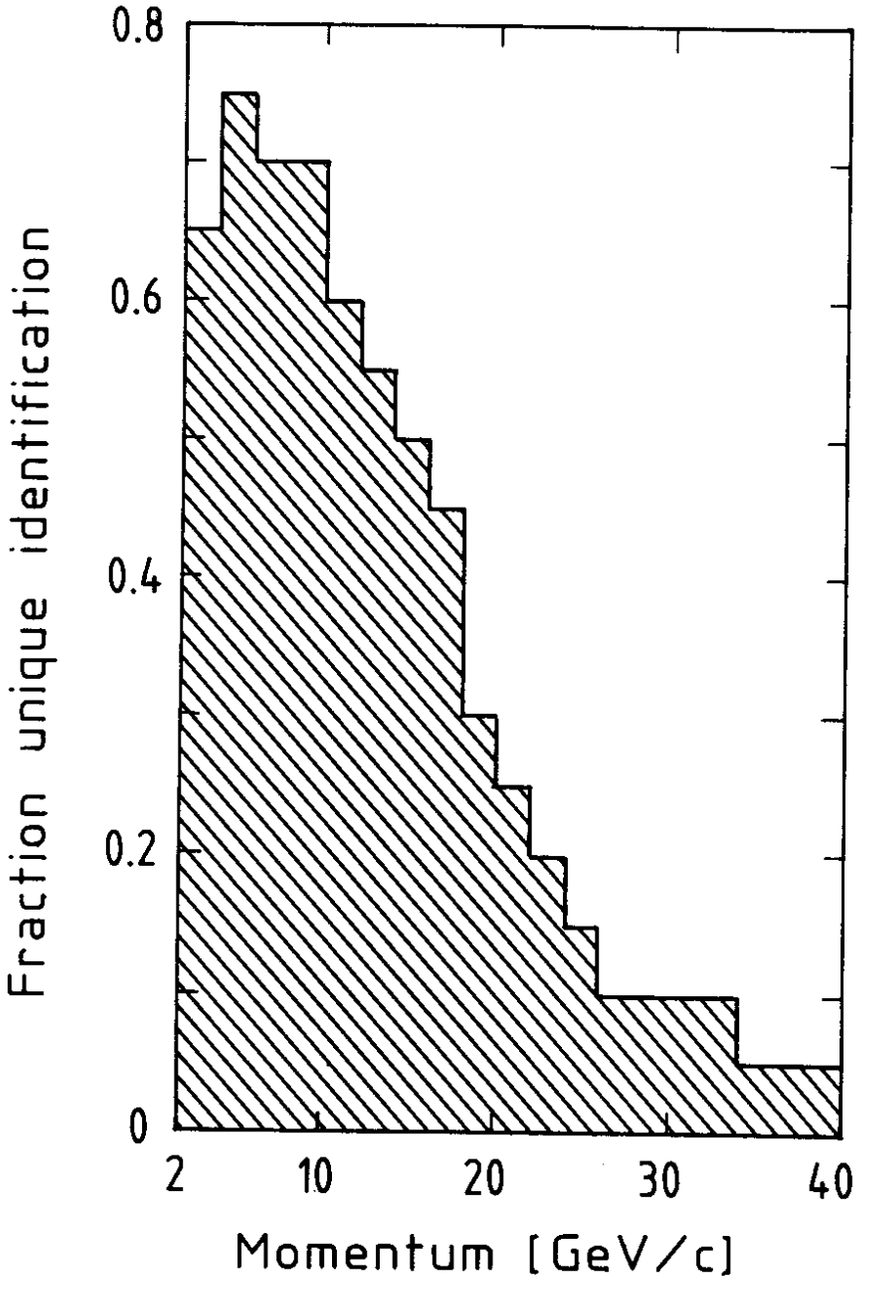
0.8
0.6
0.4
0.2
0
Fraction unique identification
2
10
20
30
40
Momentum [GeV/c]

Fig. 31